

SUPPORTING INFORMATION

Additive Transport in DNA Molecular Circuits.

Táňa Sebechlebská,^{a,Δ,§} Viliam Kolivoška,^{a,Δ} Jakub Šebera,^{a,b,Δ} Jiří Fukal,^{b,§} David Řeha,^c Miloš Buděšínský,^b Ivan Rosenberg,^b Lucie Bednářová,^b Jindřich Gasior,^a Gábor Mészáros,^d Magdaléna Hromadová,^{*a} and Vladimír Sychrovský^{b,e}

^a *J. Heyrovský Institute of Physical Chemistry of the Czech Academy of Sciences, Dolejškova 3, 18223 Prague, Czech Republic.*
E-mail: magdalena.hromadova@jh-inst.cas.cz

^b *Institute of Organic Chemistry and Biochemistry of the Czech Academy of Sciences, Flemingovo náměstí 2, 166 10, Praha 6, Czech Republic.*

^c *Center for Nanobiology and Structural Biology, Institute of Microbiology of the Czech Academy of Sciences, Zámek 136, 373 33 Nové Hradky, Czech Republic.*

^d *Research Centre for Natural Sciences, Eötvös Lóránd Research Network, Magyar Tudósok krt. 2, H-1117, Budapest, Hungary.*

^e *Department of Electrotechnology, Faculty of Electrical Engineering, Czech Technical University, Technická 2, 166 27, Praha 6, Czech Republic*

[‡] *Present address: Department of Physical and Theoretical Chemistry, Faculty of Natural Sciences, Comenius University in Bratislava, Mlynská dolina, Ilkovičova 6, 84215 Bratislava, Slovakia*

[§] *Present address: Department of Physical Chemistry, Faculty of Science, Palacký University Olomouc, tr. 17. listopadu 1192/12 771 46 Olomouc, Czech Republic*

^Δ *These authors contributed equally.*

Table of Contents

1. Chemicals and Materials	S2
2. Sample Preparation	S2
3. NMR Measurements	S3
4. CD Spectroscopy Measurements	S5
5. STM Break Junction Measurements	S6
Logarithmic Conductance–Distance Retraction Curves	S6
Characteristic Plateau Length Histograms	S7
Junction Formation Probability	S8
6. Theoretical Calculations	S9
7. STM BJ characteristics of DNA chains with one anchoring group	S20
8. References	S21

1. Chemicals and Materials

The DNA oligonucleotides 5'-CCGTGAGCC-3' (**ssDNA**), 5'-GGCTCACGG-3' with 5'-(CH₂)₆-NH₂ and 3'-CH₂CH-(CH₂OH)(CH₂)₄-NH₂ substituents (**ssDNA-NH₂**) and 5'-GGCTCACGG-3' with 5'-(CH₂)₆-S-S-(CH₂)₆-OH and 3'-(CH₂)₃-S-S-(CH₂)₃-OH substituents (**ssDNA-S**) were purchased from Generi Biotech (Czech Republic). Their chemical structures are shown in Fig. S1. Molecule **ssDNA-S** is a precursor of the DNA oligonucleotide molecule, which is generated in-situ during the STM break junction (STM-BJ) measurements via a cleavage of both disulphide bonds upon the contact with metallic gold electrodes,¹ see part of the chemical structure in brackets. In relation to STM-BJ measurements the in-situ generated molecule is also labelled **ssDNA-S** for simplicity. Most of the discussion in the main manuscript refers to **ssDNA-S** in this sense.

Nitrogen gas (99.998 %, Messer), nitric acid (65 %, p.a., Lachner, Czech Republic), sulfuric acid (96 %, p.a., Lachner, Czech Republic), hydrogen peroxide (30 %, p.a., Lachner, Czech Republic), D₂O (99.9 % D, Merck, Germany), polyethylene rods for hot glue guns (Pattex) were used as received. Gold sheet 10 mm × 10 mm × 1 mm (99.95%, GoodFellow, U.K.) was cleaned by annealing in a butane flame followed by cooling down in a stream of clean nitrogen gas. Gold wire (99.99 %, 0.25 mm in diameter, GoodFellow, U.K.) was used for preparation of the gold STM tip ultramicroelectrodes by the electrochemical etching process. Such tips were further coated by a polyethylene layer to provide sufficient insulation for experiments in the polar aqueous solvent. Ultrapure deionized water (maximum TOC of 3 ppb, minimum resistivity of 18.2 MΩ.cm) was obtained by Milli-Q Integral 5 purification system (Merck Millipore, France).

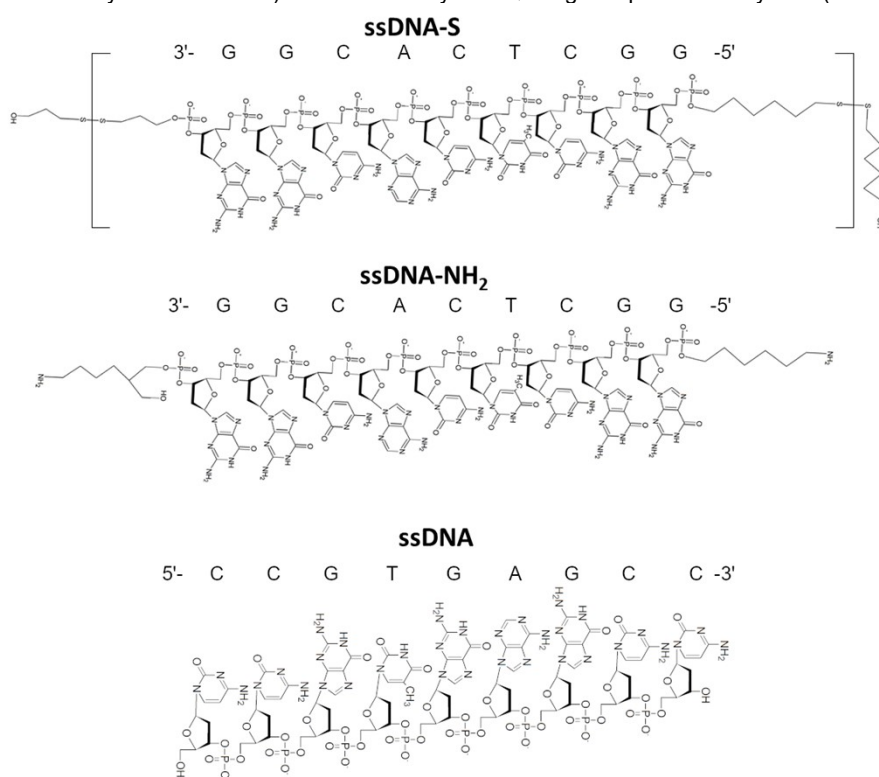


Figure S1. Chemical structures of **ssDNA-S**, **ssDNA-NH₂** and complementary **ssDNA** oligonucleotide. Structure in brackets represents molecule **ssDNA-S** formed in-situ in the STM-BJ measurement. Sodium cation per each phosphate anion is not shown.

2. Sample Preparation

For STM-BJ measurements the oligonucleotides (ca 550 nmol each) were dissolved in 1 mL D₂O giving 5.5×10⁻⁴ M stock solution of **ssDNA**, **ssDNA-NH₂** and **ssDNA-S**, respectively. The final 2.7×10⁻⁴ M solution of single stranded DNA employed in the measurements was prepared by adding 0.5 mL of D₂O into 0.5 mL of **ssDNA-NH₂** or **ssDNA-S** stock solution. The double-stranded DNA samples **dsDNA-NH₂** and **dsDNA-S** (see Figure S2) were prepared by mixing together 0.5 mL of **ssDNA** with 0.5 mL of either **ssDNA-NH₂** or **ssDNA-S** stock solution. Samples for NMR and CD spectroscopy measurements were prepared by dissolving the equimolar mixture of **ssDNA** and **ssDNA-NH₂** oligonucleotides in 1 mL of the solvent containing 95:5 (volume:volume) H₂O to D₂O ratio.

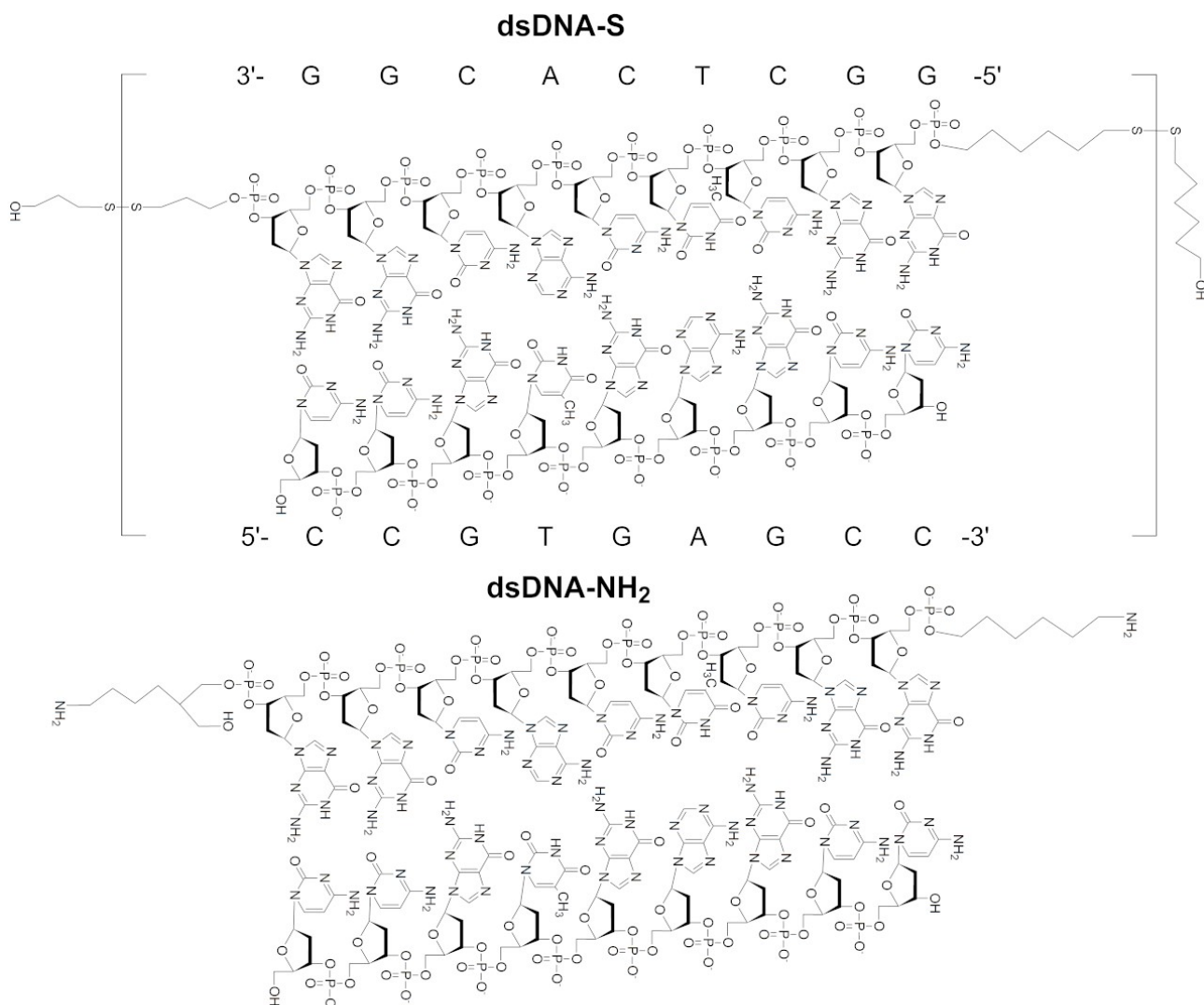


Figure S2. Chemical structure of **dsDNA-S** and **dsDNA-NH₂** duplex being held by hydrogen bonds between complementary base pairs (not shown). Structure in brackets represents molecule **dsDNA-S** formed in-situ in the STM-BJ measurement. Sodium cation per each phosphate anion is not shown.

3. NMR Measurements

Proton NMR spectra were measured on a Bruker 600 AVANCE III HD instrument (¹H at 600 MHz) equipped with 5 mm cryo-probe in the mixture of H₂O and D₂O (95:5) at 25°C. Chemical shifts were referenced to dioxane (added as internal standard) and recalculated using $\delta_{\text{H}}(\text{dioxane}) = 3.75$ ppm. Phosphorus NMR spectra were measured in the mixture of H₂O and D₂O (95:5) at 25°C on a Bruker 500 AVANCE III HD instrument (³¹P at 202.4 MHz) in 5 mm cryo-probe and referenced to H₃PO₄ as external standards. The ³¹P NMR spectrum of **ssDNA** included eight resolved singlets from +0.2 to -0.5 ppm (Fig. S3). A group of eight singlets that ranged similarly was resolved also for the **ssDNA-NH₂** plus the singlet at +1.3 ppm and the doublet at +0.9 ppm due to a racemic form of the chiral carbon atom within the linker (Fig. S3). The two upmost positive ³¹P NMR shifts were apparently due to the phosphates adjacent to NH₂-linkers as can be also inferred from the ³¹P NMR calculations (see Tab. S2 in Section 6). The formation of **dsDNA-NH₂** duplex was observed within the low-field region 10 – 15 ppm in ¹H NMR spectra due to the imino protons in nucleobases (Fig. S4). The ¹H resonances recorded only for mixture of the compatible DNA oligonucleotides clearly demonstrated H-bonded states of imino protons within the DNA duplex. The ¹H resonances broadened and shifted up-field with the increase of temperature up to ca 50°C, which indicated duplex stability at the room temperature and estimative range of temperatures of the duplex melting (Fig. S5). The very weak and broad signals around 11 ppm (marked with blue arrows in Fig. S5) are due to the imino protons within 5'- and 3'-end residues adjacent to NH₂-linkers. These signals are present only at the lowest temperature which indicated notable flexibility of the end-base pairs/residues. On the other hand, the well-resolved signals indicated H-bonded imino protons in other residues and sustainability of duplex up to the temperature range near the melting point.

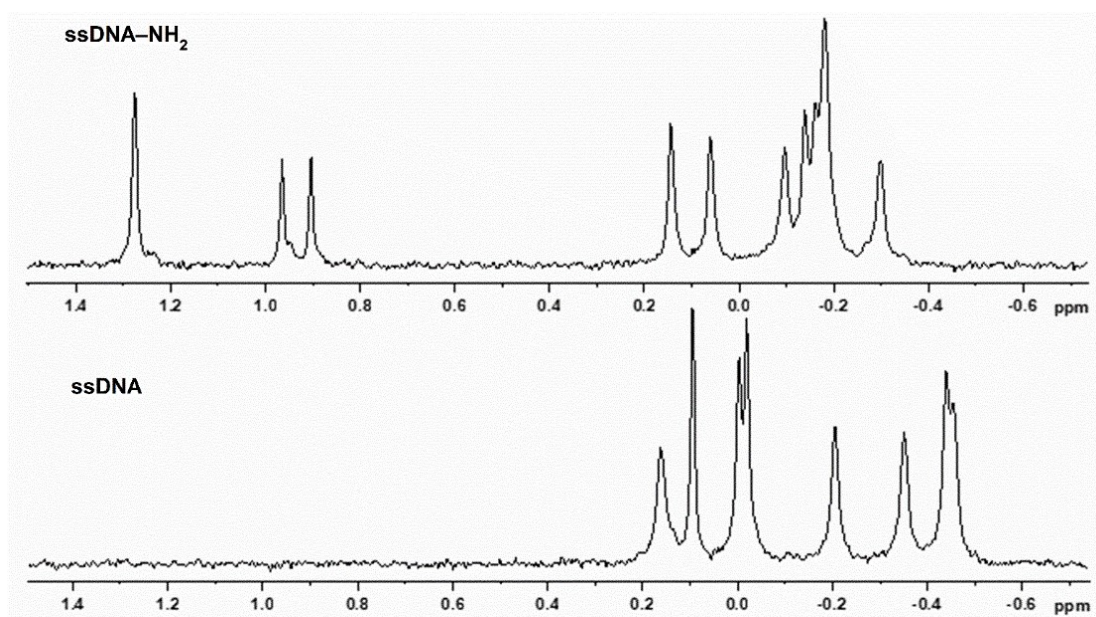


Figure S3. The ^{31}P NMR spectrum of ssDNA-NH₂ and complementary ssDNA oligonucleotides (202.4 MHz; H₂O:D₂O (95:5)).

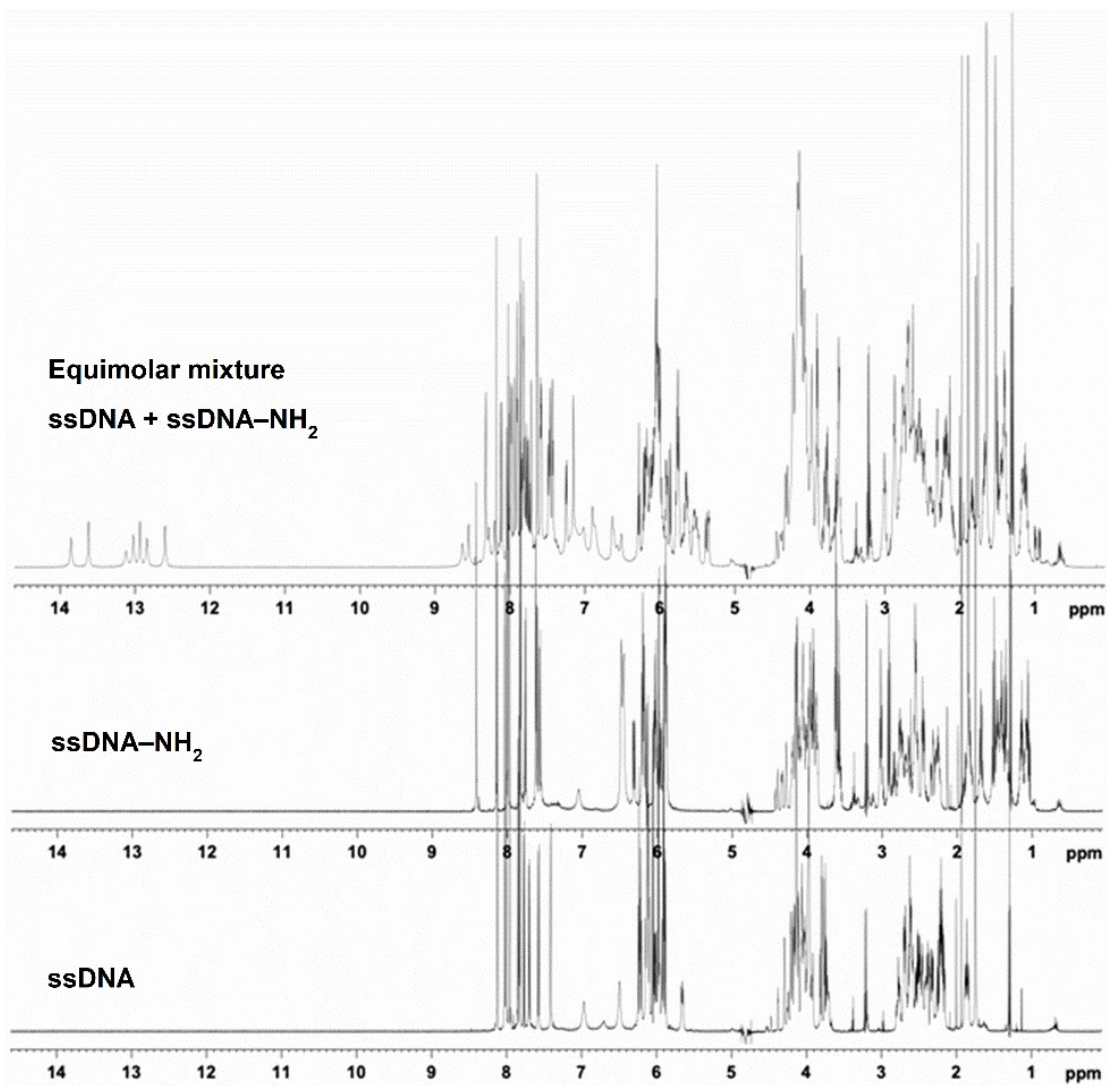


Figure S4. The ^1H NMR spectra (600 MHz; H₂O:D₂O (95:5)) of ssDNA, ssDNA-NH₂ and of their equimolar mixture.

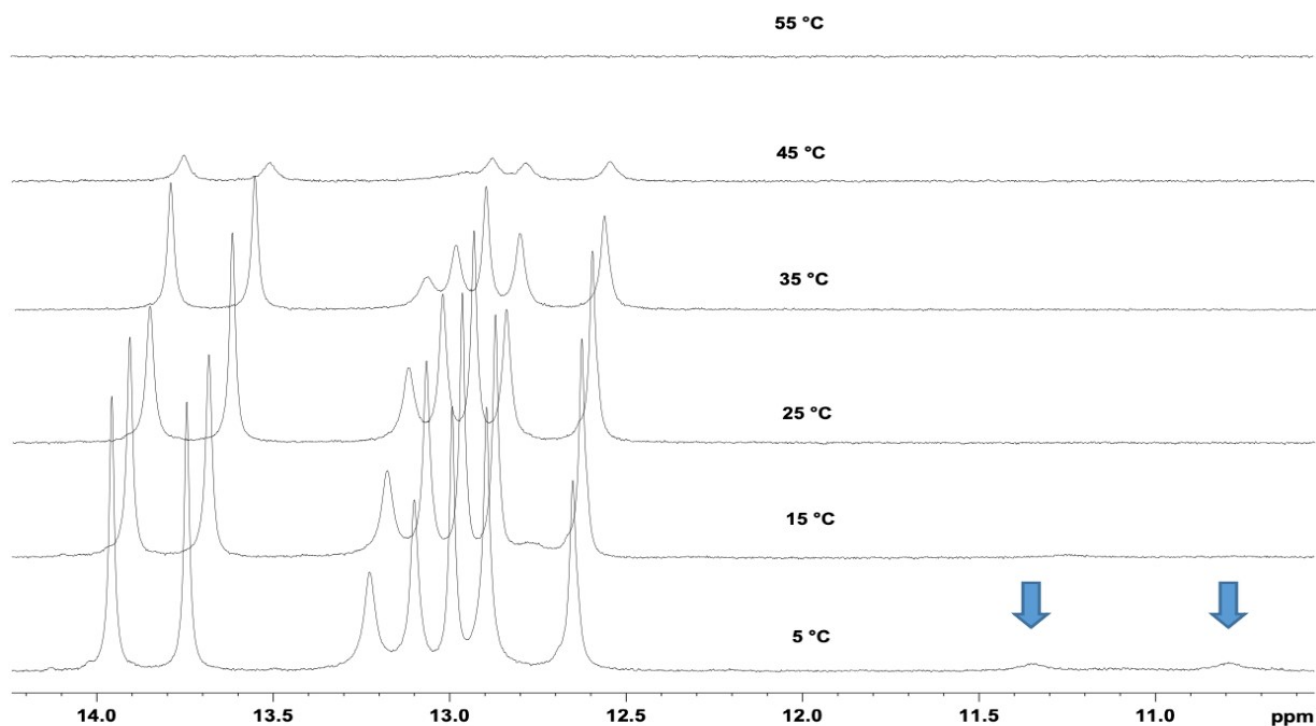


Figure S5. The temperature dependence of low-field part of ^1H NMR spectra due to imino protons in nucleobases acquired in $\text{H}_2\text{O}:\text{D}_2\text{O}$ (95:5) for equimolar mixture of **ssDNA** and **ssDNA-NH₂**. The very weak and broad signals around 11 ppm (marked with blue arrows) are due to the imino protons within 5'- and 3'-end residues adjacent to NH_2 -linkers.

4. CD Spectroscopy Measurements

The circular dichroism (CD) spectroscopy measurements were performed on a Jasco-1500 spectropolarimeter (JASCO, Easton, MD, USA). CD spectra within the range from 200 to 350 nm were recorded using cylindrical quartz cell with an optical path of 0.1 mm at room temperature, standard instrument sensitivity, 1 nm bandwidth, scanning speed of 10 nm/min, response time of 8 s, one accumulation. After baseline subtraction, the CD and absorption spectrum was expressed in differential molar extinction $\Delta\epsilon$ ($\text{L mol}^{-1} \text{cm}^{-1}$) and in molar extinction ϵ ($\text{L mol}^{-1} \text{cm}^{-1}$) per residue, respectively. The CD spectrometer allows measurement of absorption spectra in second channel. The CD spectrum with negative spectral band at 245 nm and positive spectral band at 275 nm with comparable intensities indicated B-form of the DNA duplex (Fig. S6).²

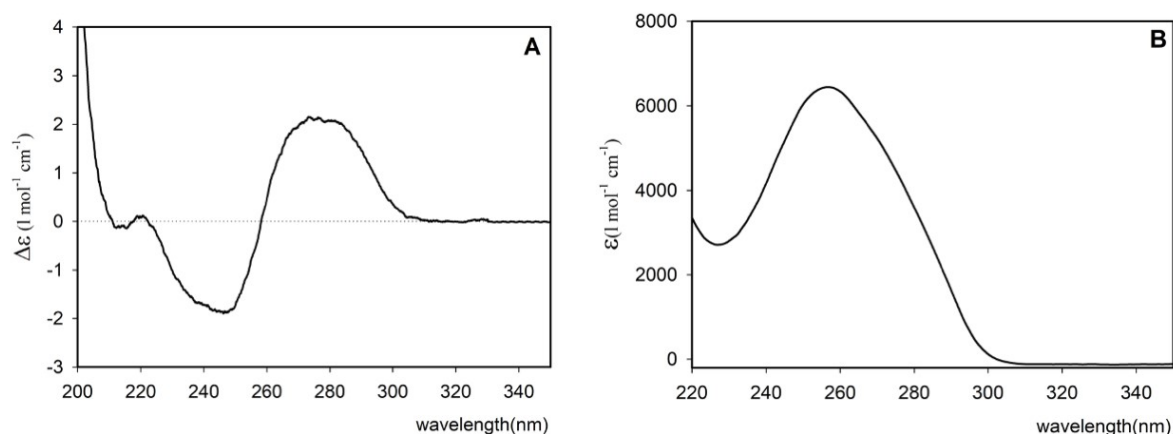


Figure S6. The CD (A) and the absorption (B) spectra of equimolar mixture of **ssDNA** and **ssDNA-NH₂** oligonucleotides at room temperature expressed in differential molar extinction $\Delta\epsilon$ ($\text{L mol}^{-1} \text{cm}^{-1}$) and in molar extinction ϵ ($\text{L mol}^{-1} \text{cm}^{-1}$) per residue.

5. STM Break Junction Measurements

STM break junction (STM-BJ) measurements were performed using Agilent 5500 Scanning Probe Microscope (Agilent Technologies, USA), where an original STM tubular scanner was fitted with a bipolar logarithmic current-to-voltage converter.^{3,4} The electric potential difference (the bias voltage) between two gold electrodes (substrate and tip) was set to 130 mV. The electric current through the junction was measured as a function of the distance between these two gold electrodes as was described in detail elsewhere.³ The STM-BJ measurements were obtained at ambient temperature and pressure. The entire experimental equipment for STM-BJ (polytetrafluoroethylene liquid cells and tweezers, Kalrez O-rings, glassware for the solution preparation and handling) was cleaned by boiling in 25% nitric acid. The acid was removed by repeated boiling of the equipment in deionized water. Such cleaned items were subsequently dried overnight at 105 °C in the oven and placed in a dust-free environment. A gold sheet 10 mm × 10 mm × 1 mm, 99.95% (GoodFellow, U.K.) was used as the substrate for single molecule conductance measurements. The substrate was cleaned by overnight immersion in freshly prepared **Piranha solution** (96 % sulfuric acid and 30 % hydrogen peroxide cautiously mixed in the volume ratio of 3:1). **Caution! Such a mixture is highly corrosive and fuming. Its preparation and handling require wearing safety goggles and gloves.** Just before measurements, the substrate was taken out of the Piranha solution, copiously rinsed with ultrapure water, annealed by a butane flame and cooled down in the stream of nitrogen and let to dry in a closed chamber.⁵ Tips for single molecule conductance measurements were prepared by electrochemical etching of the gold wire 0.25 mm in diameter. Etched tips were copiously rinsed by deionized water. To suppress capacitive and faradaic electric current contributions to the overall electric current measured in the STM-BJ setup, tips were further insulated by a polyethylene coating leaving only the etched apex exposed to the investigated solution. The quality of the tip insulation was evaluated by measuring the residual electric current between the inspected tip and the gold substrate at the bias voltage of 130 mV in the aqueous solution.⁶ Tips showing residual current less than 0.1 pA were used in the STM-BJ experiments. The 2.7×10^{-4} M solution of each DNA molecule in D₂O was introduced to the polytetrafluoroethylene cell. Kalrez O-ring between the gold substrate and the cell body provided sufficient barrier against the cell leakage. The cell assembly was completed by approaching the tip to the substrate at the rate of 1000 nm/s until the tunneling current corresponding to $10^{-3} G_0$ was reached. Then the speed of the STM tip movement enabling the formation and breaking of the junction was set to 228.5 nm/s for tip approach and 0.76 nm/s for tip retraction, respectively. Several hundreds of such measurement were accumulated for each sample to ensure statistical significance of the STM-BJ results. Each current-distance retraction curve was converted to the conductance-distance curve employing Ohm's law. All experimentally obtained data were used for the construction of 1D logarithmic conductance histograms, 2D logarithmic conductance-distance histograms and characteristic plateau length histograms according to previously described procedures.³ Charge transport characteristics of the junctions are presented as a logarithm of the conductance normalized with respect to the conductance quantum $G_0 = 77.5 \mu\text{S}$, *i.e.* as $\log(G/G_0)$. Representative logarithmic conductance-distance retraction curves for **ssDNA-S** and **dsDNA-S** molecules are shown in Fig. S7. The characteristic plateau length histograms for **ssDNA-NH₂**, **dsDNA-NH₂**, **ssDNA-S** and **dsDNA-S** molecules are shown in Figs. S8 to S11. The most probable plateau length Δz^* was obtained as a best gaussian fit of the peak positioned at the highest Δz value. The experimental MJ length value was obtained after the correction of the most probable plateau length Δz^* for a snap-back distance of 0.4 nm, $z^{\text{exp}} = \Delta z^* + 0.4$ nm.

Representative Logarithmic Conductance-Distance Retraction Curves

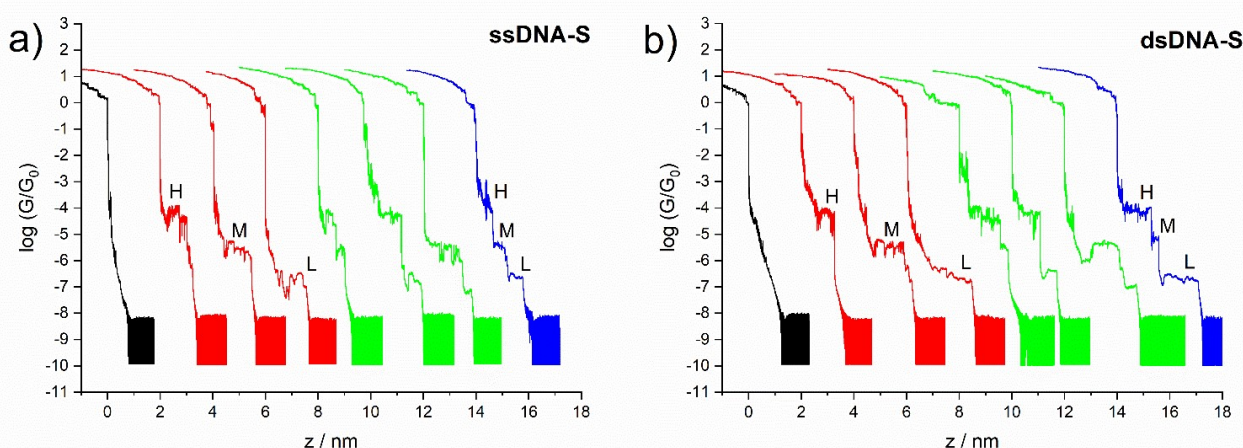


Figure S7. Representative examples of individual logarithmic conductance-distance retraction curves for **ssDNA-S** (a) and **dsDNA-S** (b) molecule, respectively. Examples include junctions with no molecules bridging the electrodes (no molecular plateau) (black), with one (red), two (green) and three (blue) molecular plateaus representing MJ configurations labeled H, M and L. Individual curves are shifted from each other on z scale by 2 nm for clarity.

Characteristic Plateau Length Histograms

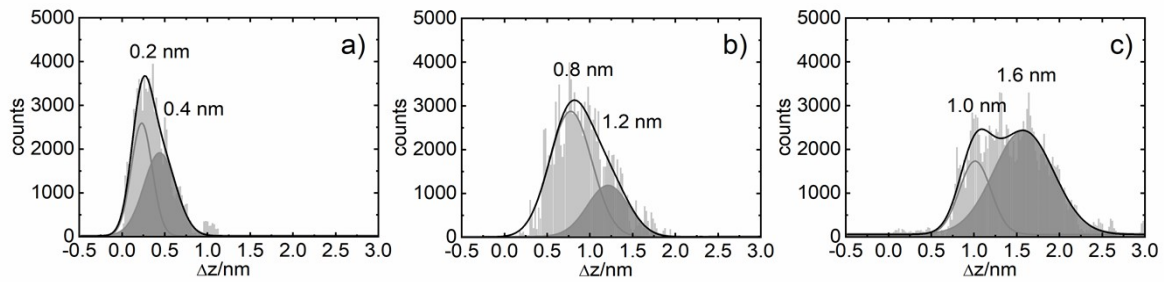


Figure S8. Characteristic plateau length Δz histogram for **ssDNA-NH₂** obtained from 2D logarithmic conductance-distance histogram as a cross-section at $\log(G/G_0)$ equal to -4.2 (a), -6.2 (b) and -7.5 (c) corresponding to H, M and L junction configurations. The most probable characteristic plateau length Δz^* is 0.4 nm (a), 1.2 nm (b) and 1.6 nm (c), respectively.

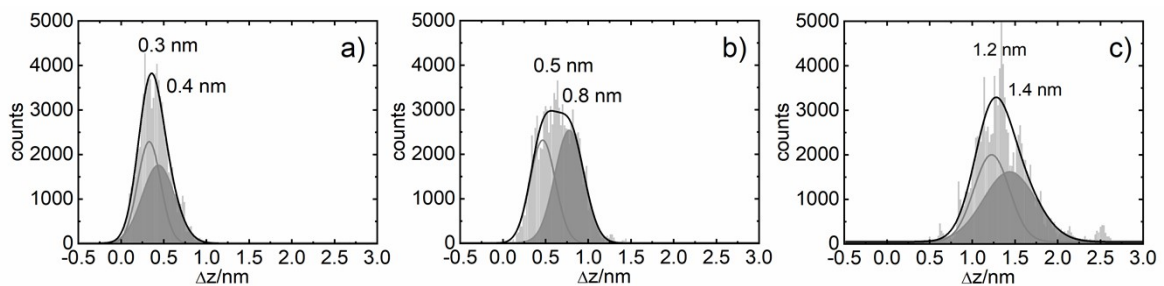


Figure S9. Characteristic plateau length Δz histogram for **dsDNA-NH₂** obtained from 2D logarithmic conductance-distance histogram as a cross-section at $\log(G/G_0)$ equal to -4.2 (a), -5.3 (b) and -7.5 (c), corresponding to H, M and L junction configurations. The most probable characteristic plateau length Δz^* is 0.4 nm (a), 0.8 nm (b) and 1.4 nm (c), respectively.

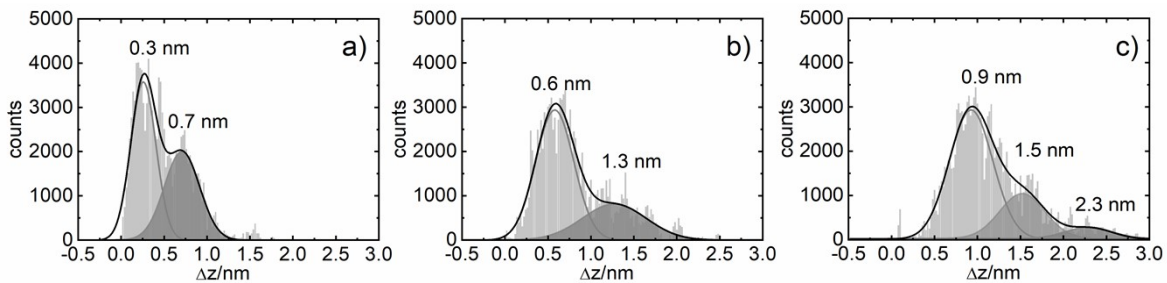


Figure S10. Characteristic plateau length Δz histogram for **ssDNA-S** obtained from 2D logarithmic conductance-distance histogram as a cross-section at $\log(G/G_0)$ equal to -4.55 (a), -6.2 (b) and -7.5 (c) corresponding to H, M and L junction configurations. The most probable characteristic plateau length Δz^* is 0.7 nm (a), 1.3 nm (b) and 2.3 nm (c), respectively.

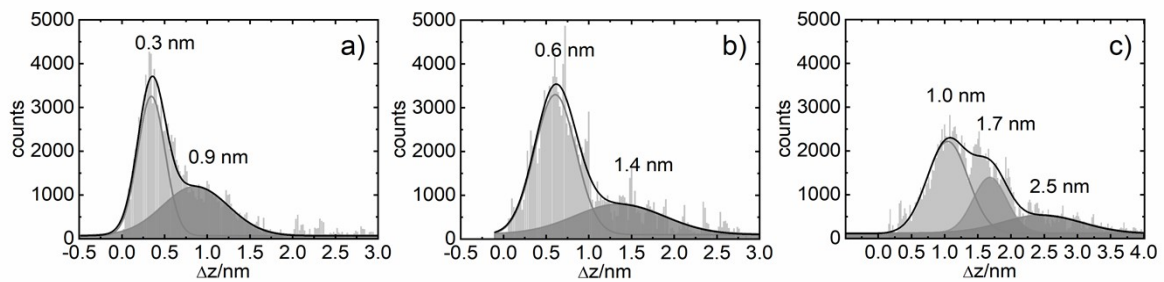


Figure S11. Characteristic plateau length Δz histogram for **dsDNA-S** obtained from 2D logarithmic conductance-distance histogram as a cross-section at $\log(G/G_0)$ equal to -4.8 (a), -5.75 (b) and -7.7 (c) corresponding to H, M and L junction configurations. The most probable characteristic plateau length Δz^* is 0.9 nm (a), 1.4 nm (b) and 2.5 nm (c), respectively.

Junction Formation Probability

Figure S12 summarizes relative abundance of 8 possible types of logarithmic conductance-distance retraction curves (see individual examples in Fig. S7) within each data set obtained by STM-BJ conductance measurement for **ssDNA-NH₂** (a), **dsDNA-NH₂** (b), **ssDNA-S** (c) and **dsDNA-S** (d) molecules. Table S1 provides statistical analysis of the retraction curves containing distinct molecular conductance plateau(s), i.e. excluding traces in which no molecular conductance plateaus were observed (excluding black column in Fig. S12). Junction formation probabilities denoted as L_{total} (M_{total} or H_{total}) specify curves in which a plateau representing the L (M or H) configuration was found within the ensemble of such retraction curves. Junction formation probabilities labelled L_{end} , M_{end} and H_{end} in Tab. S1 represent the occurrence of retraction curves ending by plateau representing the L, M and H configuration before the final junction breaking. Junction formation probabilities labelled one, two and three refer to the percentual abundance of curves with one, two and three plateaus in one logarithmic conductance-distance retraction curve.

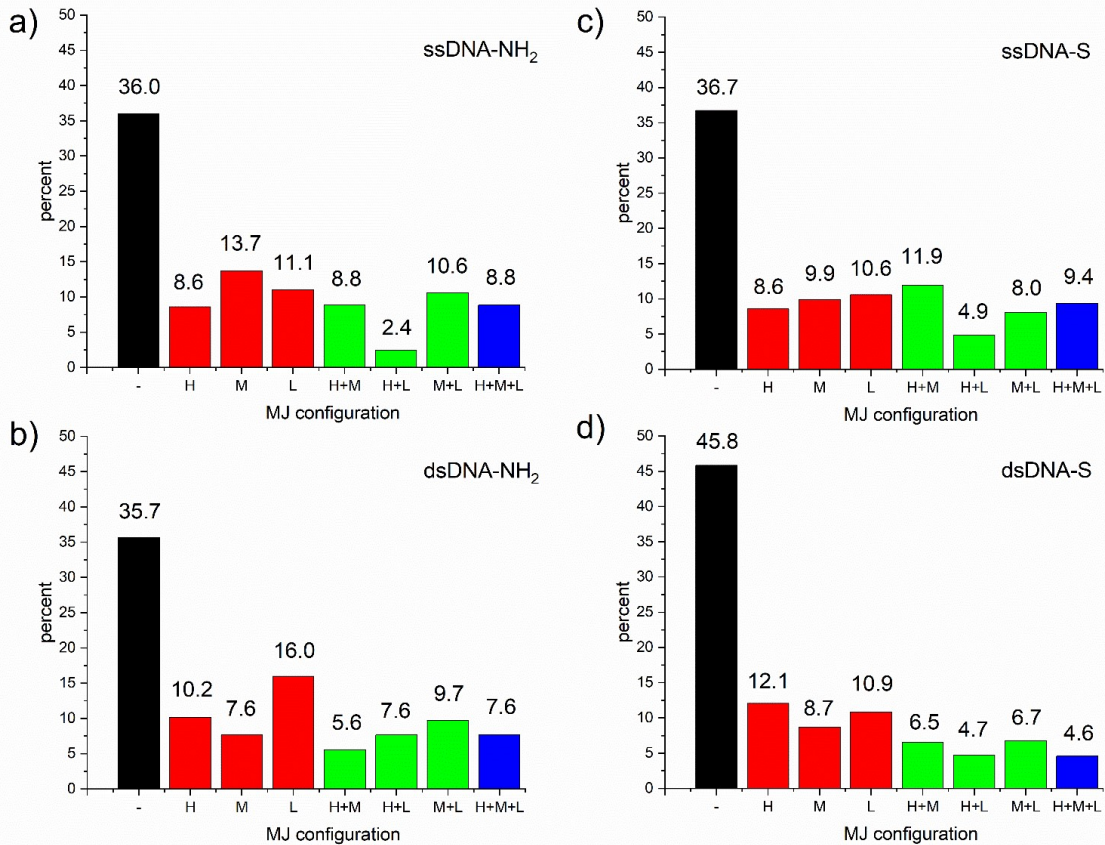


Figure S12. Junction formation probability for **ssDNA-NH₂** (a), **dsDNA-NH₂** (b), **ssDNA-S** (c) and **dsDNA-S** (d) molecules. MJ configurations: no molecules bridging the electrodes (black); one conductance plateau corresponding to H, M or L configuration (red); two conductance plateaus corresponding to H+M, H+L and M+L configurations (green) and three conductance plateaus corresponding to H+M+L configurations in one retraction curve (blue).

Table S1. The junction formation probability (%) for three DNA junction configurations labelled high (H), medium (M) and low (L) based on the occurrence of molecular plateaus in the logarithmic conductance-distance curves.

MJ ^a	L_{total} ^b	M_{total} ^b	H_{total} ^b	L_{end}	M_{end}	H_{end}	one	two	three
ssDNA-NH₂	51	66	45	51.4	35.2	13.4	52.1	34.1	13.8
dsDNA-NH₂	64	51	48	63.7	20.5	15.8	52.5	35.6	11.9
ssDNA-S	52	62	55	52.0	34.5	13.5	45.8	39.3	14.8
dsDNA-S	50	49	51	49.7	28.0	22.3	58.3	33.2	8.5

^a junction formation probability in percent within the ensemble of MJs (retraction curves) containing molecular plateaus

^b percentage refers to total number of retraction curves, where one curve can contain more than one molecular plateau

6. Theoretical Calculations

The MJ conductance was calculated with the density functional tight binding (DFTB)⁷ method within the non-equilibrium Green's function (NEGF)⁸ approach (DFTB/NEGF)⁹ using the DFTB program¹⁰ for the DNA junction involving GG dinucleotide anchored to the gold electrodes via linkers terminated with thiolate (**ssDNA(GG)-S**) or amino (**ssDNA(GG)-NH₂**) anchoring groups. The effect of the molecular dynamics (MD) was included. MD employing the Gromacs¹¹ was calculated for the **ssDNA(GG)-S** molecule anchored via S-linkers to gold electrodes, where each Au(111) electrode¹² included 2000 atoms. Positions of the gold atoms were fixed whereas their dipoles were allowed to oscillate as described in detail elsewhere.¹³ Water used as solvent included Na⁺ ions to compensate the negative charges of the DNA phosphates. The TIP3P model was used to simulate the water environment. The distance between the electrodes was set to 1.9 nm (Fig. S13).

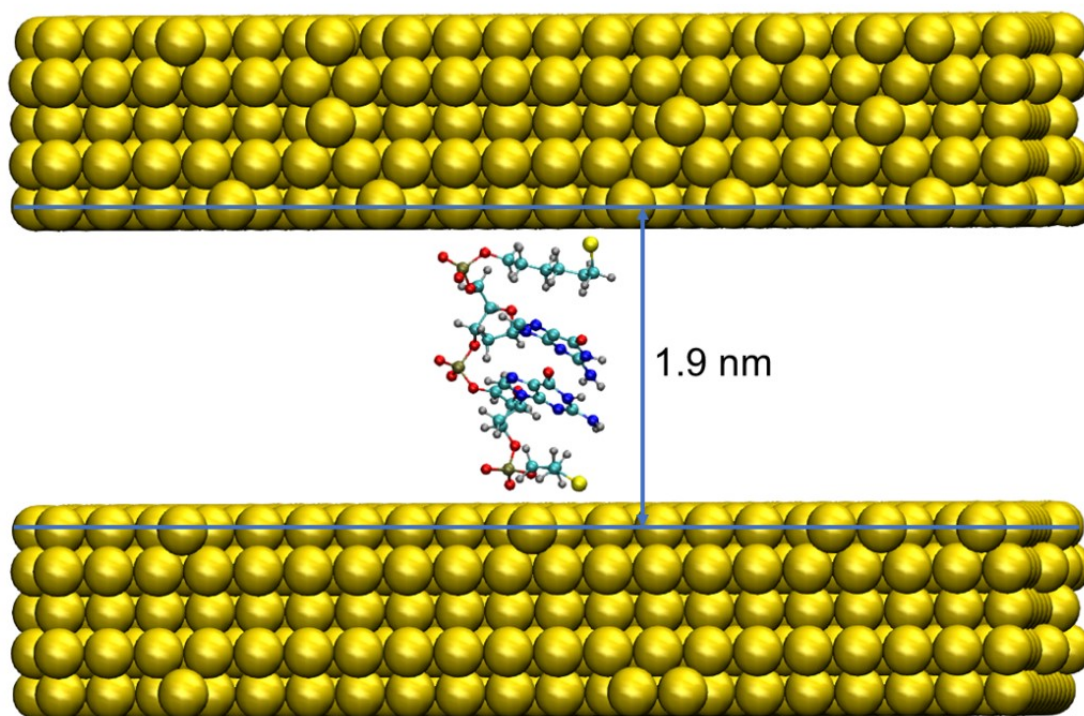


Figure S13. Molecular junction of **ssDNA(GG)-S** employed in MD calculation (the snapshot of an equilibrated system taken at 0 ns MD run) involving GG oligonucleotide anchored via S-linkers to the gold electrodes containing each 2000 atoms. Na⁺ ions and water molecules are not shown. The electrode–electrode distance 1.9 nm corresponding to the length of DNA junction was constrained in MD calculations.

The system minimized with the steepest descent method was equilibrated within 100 ps NVT MD where all heavy atoms were restrained with the force constant 1000 kJ mol⁻¹ nm⁻². The production MD included 10 ns NVT. In total 11 snapshots were taken at 0, 1, 2, ... and 10 ns of the MD run. For NH₂ group adsorbed at the gold surface an adequate force field is unavailable to the best of our knowledge. Therefore, S-linkers in the MD snapshots were replaced by the NH₂-linkers using the GaussView program.¹⁴ Subsequent DFTB/NEGF calculations employed snapshots with smaller electrodes, each involving 108 Au atoms (Au₁₀₈ electrodes), see Fig. S14. The replacement of larger electrodes in MD by the Au₁₀₈ electrodes was done using the Maestro 9.3 program.¹⁵ All the snapshots were geometry optimized with the DFTB employing the extended tight-binding (GFN1-xTB) Hamiltonian that includes dispersion correction.¹⁶ First optimization involved DNA junction with the charge -3 due to phosphate groups with fixed positions of gold atoms in Au₁₀₈ electrodes. Then, only the geometries of three Na⁺ counterions added to the DNA phosphates were geometry optimized. The geometry-optimized snapshots of electro-neutral system involving equidistant Au₁₀₈ electrodes were employed in DFTB/NEGF calculations of the transmission function assuming coherent tunneling charge transport. The MJ conductance G was calculated according to the Landauer equation; $G = T(E_F)G_0$, where $T(E_F)$ is the value of the transmission function at the Fermi level E_F of gold electrodes and G_0 is the conductance quantum.¹⁷ The G was calculated with the QUASINANO2013.1 parameters¹⁸ that were employed successfully within the DFTB/NEGF recently.¹⁹ Theoretical conductance of the DNA was calculated as an average conductance in 11 snapshots for each of the two anchoring groups including linkers, see Figure S17. For **ssDNA(GG)-NH₂** molecular junctions $\log(G/G_0)$ ranged from -11.18 to -9.08 and the averaged conductance was $\log(G/G_0) = -9.9 \pm 0.7$. For **ssDNA(GG)-S** molecular junctions $\log(G/G_0)$ ranged from -10.97 to -8.91 and the averaged conductance was $\log(G/G_0) = -9.9 \pm 0.6$. To study the effect of sugar phosphodiester backbone on the charge transport in DNA molecules, we performed calculations where the model **ssDNA(GG)-S** junction was replaced by the model where DNA bases were omitted (**ssDNA(abasic)-S**) and the glycosidic bond was modelled by C1'-H bond. All geometry-optimized 11 snapshots were modified for this model. The hydrogens were re-optimized by the GFN1-xTB DFTB method and positions of all remaining

atoms were fixed at their xyz coordinates as calculated for **ssDNA(GG)–S** model. Then, the conductance was calculated by DFTB/NEGF method as explained above. For this model, the DNA conductance $\log(G/G_0)$ ranged from -12.56 to -9.14 and the averaged logarithmic conductance was -10.3 ± 1.0 . Our model predicts that the efficiency of CT through **ssDNA(GG)–S** molecular junction is indeed more effective than in the model where the DNA bases are omitted.

The geometry-optimized snapshots with the charge -3 were employed in DFTB calculation of the interaction energy E_{int} due to the adsorbed DNA on Au_{108} electrodes. $E_{\text{int}} = E_{\text{complex}} - (E_{\text{GG}} + E_{\text{Au}_{108}})$, where E_{complex} is the energy of the system, E_{GG} is the energy of either **ssDNA(GG)–S** or **ssDNA(GG)–NH₂** molecule, $E_{\text{Au}_{108}}$ is the energy of Au_{108} electrodes. E_{int} was also calculated as an average energy of 11 snapshots for each of the two linkers, see Fig. S15. For NH_2 – anchoring, the E_{int} ranged from -278.0 kcal mol⁻¹ to -195.1 kcal mol⁻¹ and the averaged E_{int} value was -222.4 ± 23.4 kcal mol⁻¹. For S– anchoring, the E_{int} ranged from -303.9 kcal mol⁻¹ to -194.0 kcal mol⁻¹ and the averaged E_{int} value was -267.2 kcal mol⁻¹.

Degree of the stacking of nucleobases within the **ssDNA(GG)–S** junction (Fig. S13) was resolved with the geometrical parameters described elsewhere.²⁰ The distance between glycosidic nitrogen atoms smaller than 6.4 Å, angle between in-plane vectors (N9→C6) of adjacent GG nucleobases must not exceed 60 degrees and angle between the planes of GG nucleobases must not exceed 45 degrees can be regarded as reliable indicators of stacked adjacent nucleobases (Fig. S16). Based on the above explained criteria, we can argue that base-base stacking between GG base pairs is partially disrupted during the duration of the molecular dynamic simulation.

The MJ configurations for **ssDNA-S** and **dsDNA-S** molecules were calculated using MD simulations in Gromacs. The Au(111) gold electrode was represented by 5445 gold atoms. Calculations for MJ configurations of DNA molecules between two gold electrodes started with the electrode-to-electrode distance of 4.8 nm (the definition of the distance corresponds to the situation shown in Fig. S13) and stepped to shorter distances. Each step consisted of minimization, 100 ps NVT equilibration and 10 ns NVT production run, all in standard laboratory conditions (temperature 300 K). The calculation of dsDNA molecule started at 4.80 nm and continued gradually with the distances 4.65, 4.50, 4.35, 4.20, 4.05, 3.90, 3.75, 3.60, 3.45, 3.30, 3.15, 3.00, 2.89, 2.70 and 2.50 nm distance. The last distance was not calculable, so we continued with a MJ geometry of laying dsDNA molecule. The distances of gold electrodes were decreasing in the following manner: 2.30, 2.15, 2.05, 2.00, 1.80, 1.60, 1.55, 1.40, 1.30, 1.10 and 0.90 nm. The MJ configuration of single stranded DNA molecule was derived from that of dsDNA configuration at 3.15 nm, and the calculation continued gradually using the electrode distances of 2.95, 2.75, 2.55, 2.35, 2.15, 2.05, 1.95, 1.75, 1.55 and 1.35 nm. In all steps, the last snapshot from 10 ns production phase of MD simulation was used as an estimated geometry for a next step in the scan of gradual shortening of the distances between the electrodes. Finally, the last snapshot from 10 ns MD simulation was chosen to represent the DNA MJ configuration between the gold electrodes at distances obtained from the STM-BJ experimental data, see Fig. 4 in the main text.

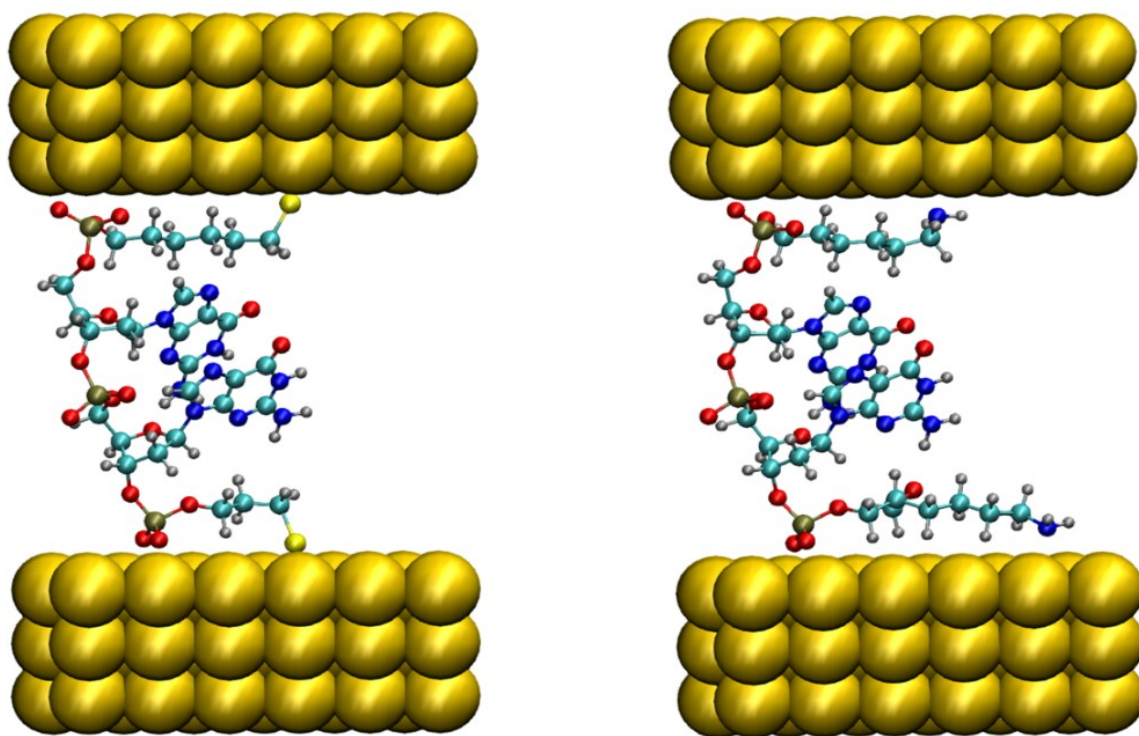


Figure S14. The **ssDNA(GG)–S** (left) and **ssDNA(GG)–NH₂** (right) junction configurations employed in DFTB/NEGF calculation of transmission functions using DFTB geometry optimized snapshots taken at 0 ns of MD simulation. Au_{108} electrodes were employed. Sodium counterions are not shown.

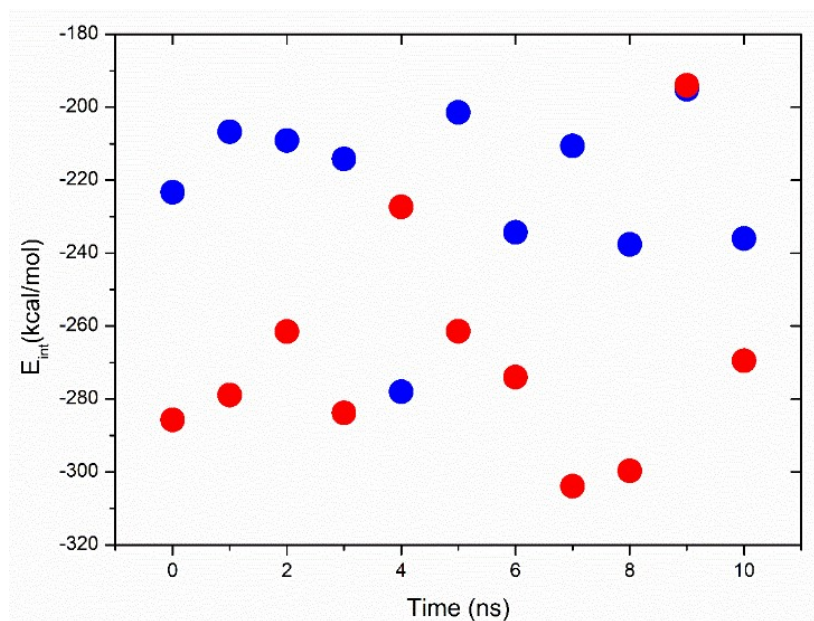


Figure S15. The interaction energies of **ssDNA(GG)-S** (red circles) and **ssDNA(GG)-NH₂** (blue circles) attached to Au₁₀₈ electrodes obtained using DFTB geometry optimized snapshots taken at 0,1,2, ... and 10 ns of the MD simulation (see Fig. S14 for 0 ns).

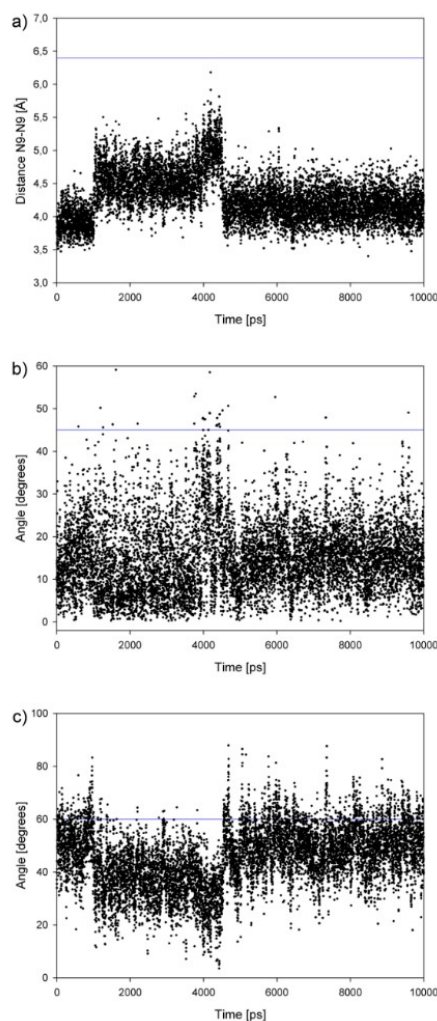


Figure S16. Evaluation of stacking in **ssDNA(GG)-S** junction (Fig. S13) throughout 10 ns MD simulation employing distance between the glycosidic nitrogen atoms (a), angle between the planes of G nucleobases (b) and angle between the N9→C6 vectors (c). Values of three geometrical parameters larger than the thresholds (blue lines) indicate loss of the GG stacking.

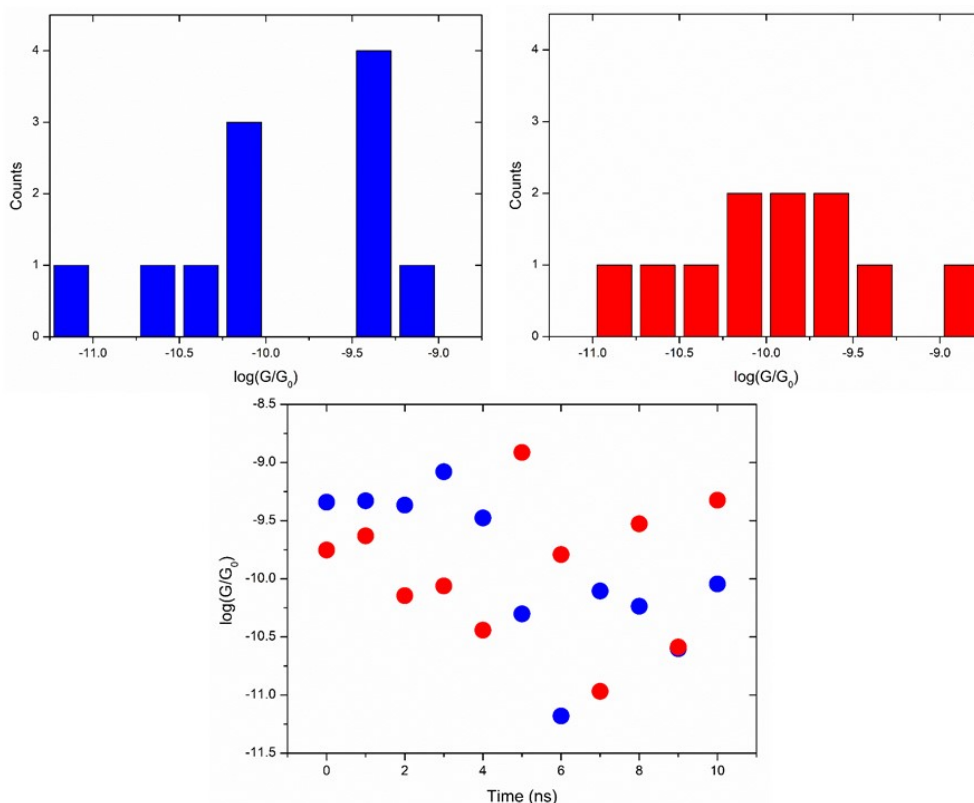


Figure S17. The histograms of $\log(G/G_0)$ values (top) obtained by DFTB/NEGF and the time evolution of $\log(G/G_0)$ values calculated in 11 snapshots taken at 0, 1, ..., 10 ns of MD run (bottom). The $\text{ssDNA}(\text{GG})\text{-NH}_2$ molecule was attached to Au_{108} electrodes via NH_2^- anchoring groups (top-left, blue circles at the bottom) and $\text{ssDNA}(\text{GG})\text{-S}$ molecule via S- anchoring groups (top-right, red circles at the bottom).

Frontier molecular orbitals contributing to the charge transport pathways and transmission functions for $\text{ssDNA}(\text{GG})\text{-S}$ and $\text{ssDNA}(\text{GG})\text{-NH}_2$ model molecular junctions are shown in Figs. S18 to S20. The highest occupied molecular orbitals (HOMO, HOMO-1, HOMO-2) were calculated by DFT-B3LYP method²¹ in Gaussian 16 program²² using 6-31G(d) basis set for all light atoms²³ and LANL2DZ²⁴ basis set including relativistic pseudopotential and relevant basis set for valence orbitals of Au atoms for system $\text{Au}_3\text{-molecule-Au}_3$ (based on the MD/DFTB calculated geometry taken from 0 ns MD simulation) in which either $\text{ssDNA}(\text{GG})\text{-S}$ or $\text{ssDNA}(\text{GG})\text{-NH}_2$ molecule was employed. The HOMO orbital of $\text{ssDNA}(\text{GG})\text{-NH}_2$ and $\text{ssDNA}(\text{GG})\text{-S}$ molecular junction is mainly localized on gold clusters and in the case of $\text{ssDNA}(\text{GG})\text{-S}$ it is localized on the anchoring group as well, see Fig. S18. Thus, we assume that main charge transport pathway for $\text{ssDNA}(\text{GG})\text{-NH}_2$ and $\text{ssDNA}(\text{GG})\text{-S}$ is mediated through HOMO-1 orbital which is localized on molecule, mainly on the DNA bases. The shape of HOMOs of the $\text{ssDNA}(\text{GG})\text{-NH}_2$ and $\text{ssDNA}(\text{GG})\text{-S}$ system was calculated using small isovalues (0.002) as well, see Fig. S19. The differences in the MO shapes due to different isovalues strongly indicate that CT mechanism interpreted using only the shapes of molecular orbitals can be misleading. The MOs for $\text{ssDNA}(\text{abasic})\text{-S}$ system representing “backbone states” are depicted in Fig. S20. Orbitals are localized mainly on the gold clusters, on linkers and on the phosphate group. What is surprising is that even if the conductance of $\text{ssDNA}(\text{abasic})\text{-S}$ system is lower than the conductance of $\text{ssDNA}(\text{GG})\text{-S}$ system, their conductance values are quite close in magnitude. The summary of HOMO orbital energies and LUMO-HOMO gap values is given in Tab. S2. Recently, Pauly *et al.*²⁵ calculated the differences in the conductance between peptide wires with and without the presence of tryptophane amino acid using the same DFT/NEGF approach as in this work. Their results show that peptide wires have virtually the same conductance independent of the presence of pendant tryptophane amino acid (aromatic moiety) on the polypeptide chain. Tryptophane amino acid does not influence strongly transport process and low electrode-molecule coupling to the frontier orbitals. In other words, the strongly localized MOs (localized on tryptophane amino acid) do not have an effect on the charge transport properties of the system as previously assumed. This may be an explanation for experimental observations provided in this work too, where a sugar phosphodiester wire (non-aromatic backbone) is decorated by pendant aromatic DNA bases. The transmission functions calculated by DFTB/NEGF method for $\text{ssDNA}(\text{GG})\text{-NH}_2$, $\text{ssDNA}(\text{GG})\text{-S}$ and $\text{ssDNA}(\text{abasic})\text{-S}$ MJ systems are depicted in Fig. S21. One can see that $\text{ssDNA}(\text{abasic})\text{-S}$ system shows large energetic gap between peaks located near the Fermi level which decreases the calculated conductance in comparison with $\text{ssDNA}(\text{GG})\text{-NH}_2$ and $\text{ssDNA}(\text{GG})\text{-S}$ systems.

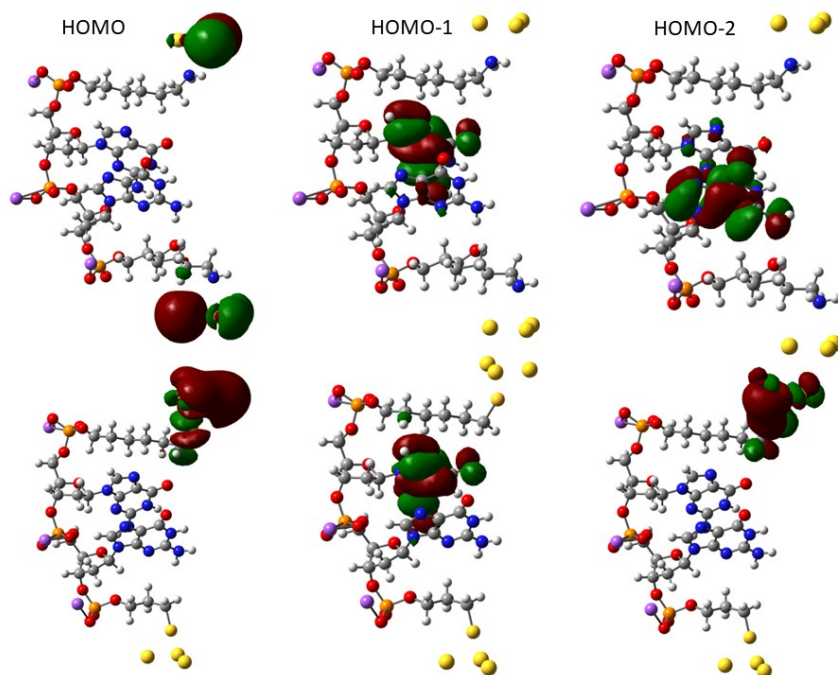


Figure S18. Summary of the highest occupied molecular orbitals for **ssDNA(GG)-NH₂** (top panel) and **ssDNA(GG)-S** (bottom panel) systems. The HOMO, HOMO-1 and HOMO-2 orbitals are based on the geometry-optimized structure taken from MD 0 ns snapshot and depicted using isovalue of 0.02.

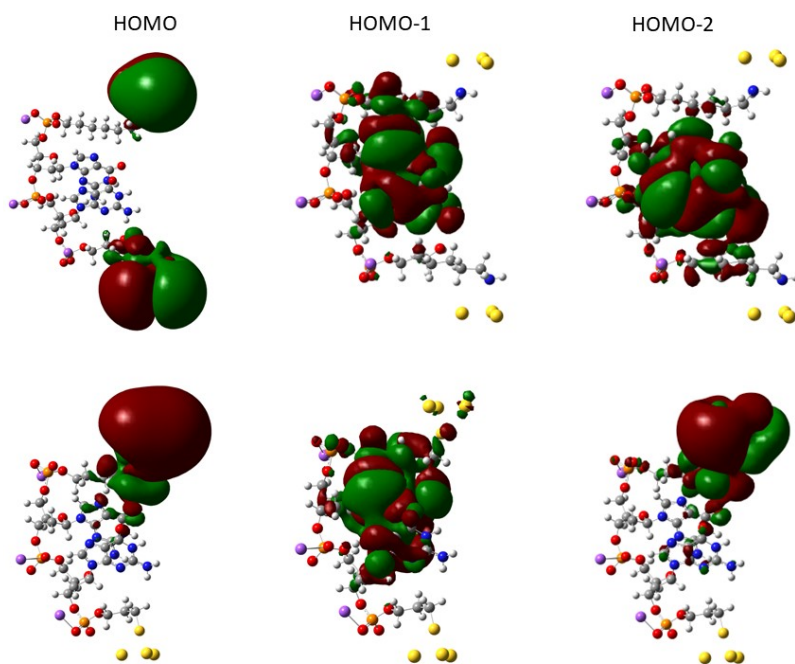


Figure S19. Summary of the highest occupied molecular orbitals for **ssDNA(GG)-NH₂** (top panel) and **ssDNA(GG)-S** (bottom panel) systems. The HOMO, HOMO-1 and HOMO-2 orbitals are based on the geometry-optimized structure taken from MD 0 ns snapshot and depicted using isovalue of 0.002.

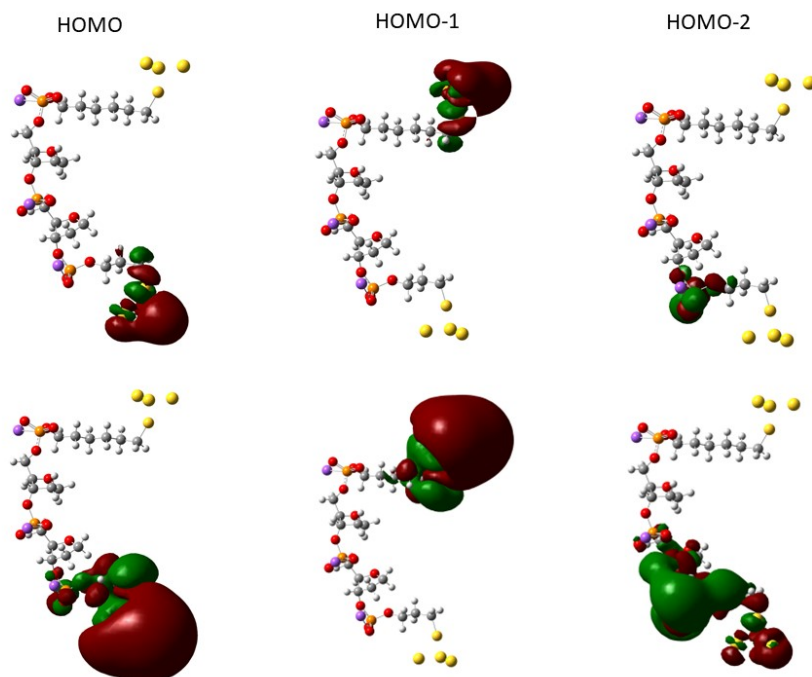


Figure S20. Summary of the highest occupied molecular orbitals for **ssDNA(abasic)-S** system using either 0.02 (top panel) or 0.002 (bottom panel) isovalues. The HOMO, HOMO-1 and HOMO-2 orbitals are based on the geometry-optimized structure taken from MD 0 ns snapshot.

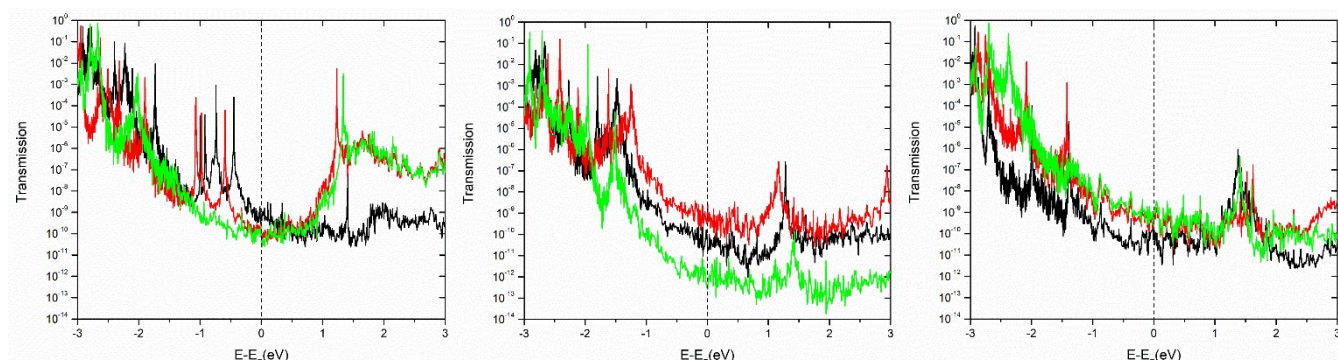


Figure S21. DFTB/NEGF calculated transmission functions of **ssDNA(GG)-NH₂** (black), **ssDNA(GG)-S** (red) and **ssDNA(abasic)-S** (green) junctions based on geometries taken from trajectory at the time of 0 ns (left), 5 ns (middle) and 10 ns (right) MD simulation.

Table S2. Summary of molecular orbital (HOMO, HOMO-1, HOMO-2) energies and LUMO-HOMO energy gap values for **ssDNA(GG)-NH₂**, **ssDNA(GG)-S** and **ssDNA(abasic)-S** system.

MJ	$E_{\text{HOMO}} / \text{eV}$	$E_{\text{HOMO-1}} / \text{eV}$	$E_{\text{HOMO-2}} / \text{eV}$	$E_{\text{LUMO-HOMO}} / \text{eV}$
ssDNA(GG)-NH₂	-3.94	-5.05	-5.37	0.15
ssDNA(GG)-S	-4.87	-5.15	-5.65	1.43
ssDNA(abasic)-S	-5.41	-5.50	-5.51	2.00

Structurally dynamical behavior of **ssDNA-NH₂** and **dsDNA-NH₂** in the absence of the gold electrodes was calculated by MD using the AMBER 14²⁶ by employing the OL15²⁷ force field for DNA. The NH₂⁻ anchoring groups and linkers were parametrized for AMBER force field employing the RESP charges with the HF/6-31G(d) for the B3LYP²¹/6-31+G(d)²⁸ geometries in a gas phase. All the calculations were performed with the Gaussian 09 program.²⁹ The DNA in MD was treated as electroneutral due to added Na⁺ counterions. The TIP3P water was used. The box for **dsDNA-NH₂** and **ssDNA-NH₂** was 58 Å × 63 Å × 76 Å and 56 Å × 60 Å × 75 Å, respectively. The equilibration included minimization of solvent followed by 100 ps NVT heating of the system to 300 K involving the restraints 25 kcal mol⁻¹ Å⁻². Then, the restraints were gradually removed within 5, 4, 3, 2, 1, 0.5 kcal mol⁻¹ Å⁻² consecutive steps, each involved minimization

plus 50 ps NPT MD equilibration. The production 100 ns NPT MD simulation was carried out without restraints. The summary of the main results is depicted in the Figs. S22 and S23.

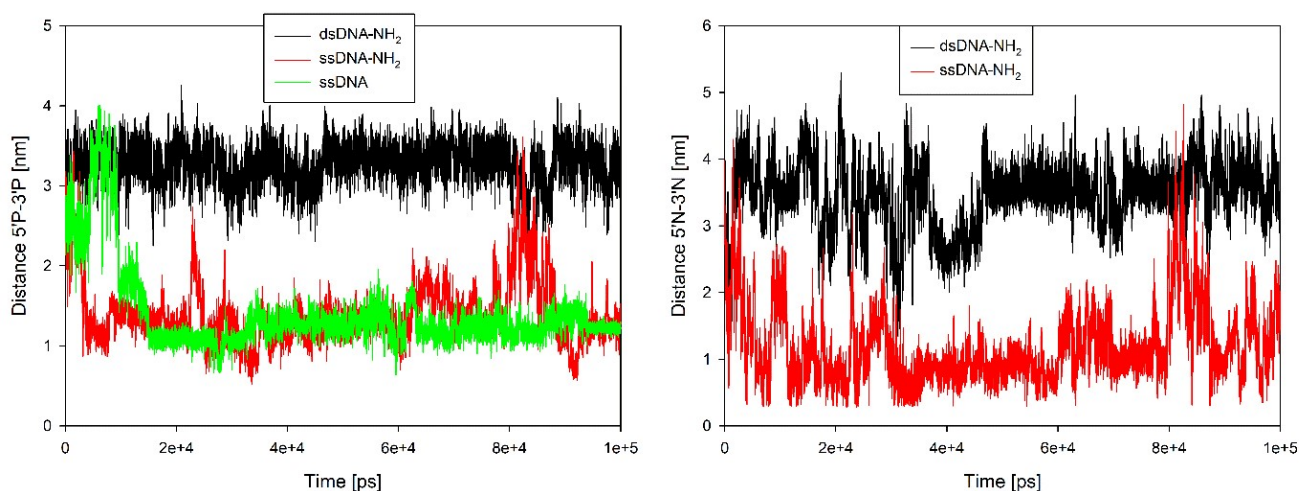


Figure S22. Time evolution of distances between the phosphorus atoms within 5' and 3' phosphates (left) and the nitrogen atoms within NH_2^- anchoring groups (right). The MD calculations for **dsDNA-NH₂** (black), **ssDNA-NH₂** (red) and **ssDNA** (green).

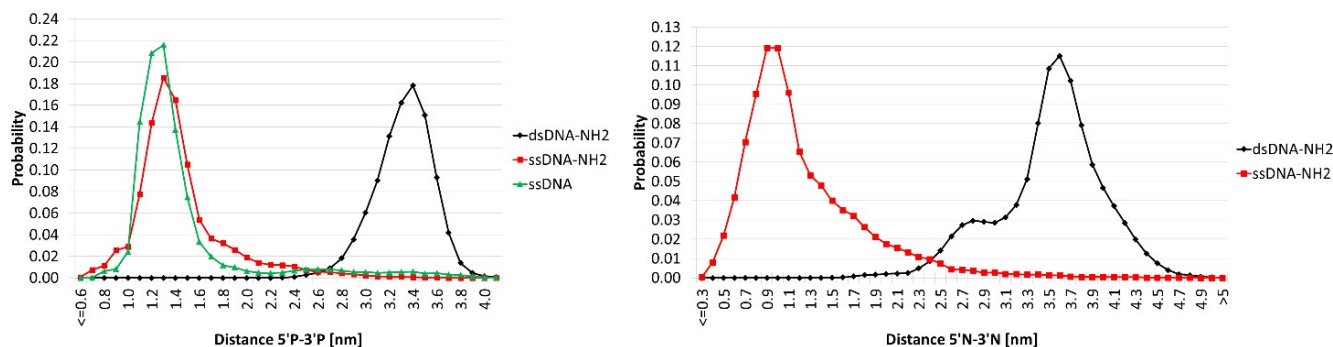


Figure S23. Probability of occurrence for particular interatomic distances between the phosphorus atoms within 5' and 3' phosphates (left) and the nitrogen atoms within NH_2^- anchoring groups (right) calculated throughout the MD simulations. The MD calculations for **dsDNA-NH₂** (black), **ssDNA-NH₂** (red) and **ssDNA** (green).

The ^{31}P NMR calculations distinguishing the inner DNA phosphate and terminal 5'- or 3'-phosphate connected through the linker to NH_2 anchoring group (Tab. S3) employed molecular models shown in Fig. S24. Their geometries corresponding to predominantly occurring conformation; the *g-g* conformer (Figs. S25 and S26), $\zeta \approx 260^\circ$ and $\alpha \approx 300^\circ$ (Fig. S24), were geometry optimized with the B3LYP method^{21,30}, 6-31++G(d) basis³¹ employing the SMD solvent³² of water. The NMR calculations employed the same method, except for the atomic basis that was Iglö-III³³. The calculations were performed with the Gaussian 09 program.²⁹ The computational procedure of these NMR calculations is described in more detail elsewhere³⁴.

Table S3. The ^{31}P NMR parameters calculated in three chemically different phosphates of the DNA with NH_2 anchoring groups.

Phosphate ^a	ζ	α	$\sigma_{31\text{P}}$ ^b	$\delta_{31\text{P}}$ ^c
sPs	260.9	303.9	292.18	0.00
$\text{NH}_25'\text{-Ps}$	267.2	303.9	290.70	1.48
$\text{NH}_23'\text{-Ps}$	260.9	290.5	291.92	0.26

^a Models of the phosphate employed in calculations: the inner DNA phosphate involving sugar-phosphate-sugar (sPs), the 5'-phosphate involving NH_2 -linker-5'-phosphate-sugar ($\text{NH}_25'\text{-Ps}$) and the 3'-phosphate involving NH_2 -linker-3'-phosphate-sugar ($\text{NH}_23'\text{-Ps}$). The ζ and α torsion angles adjacent to the phosphorus atom calculated with MD indicated dominant occurrence of the *g-g* conformation for both the 3' and the 5'-phosphate (Figs. S25 and S26).

^b Calculated ^{31}P NMR shielding in ppm.

^c Calculated ^{31}P NMR shift relative to the sPs phosphate in ppm; $\delta_{31\text{P}} = \sigma_{31\text{P}}(\text{in sPs}) - \sigma_{31\text{P}}(\text{in } \text{NH}_2\text{-linker-Ps})$.

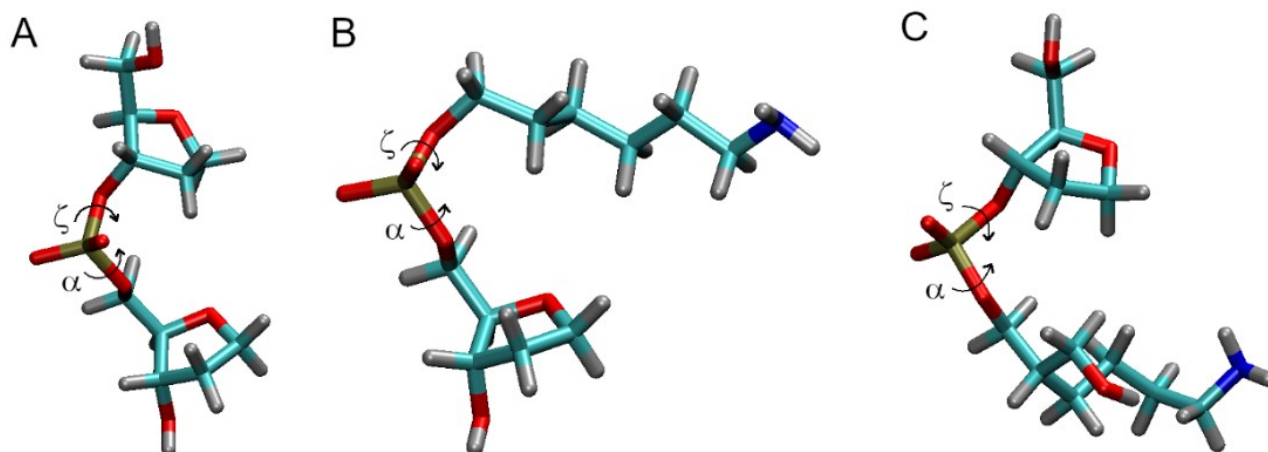


Figure S24. The sPs (A), $\text{NH}_2 5'$ -Ps (B) and $\text{NH}_2 3'$ -Ps (C) phosphates in the DNA involving NH_2 -linkers. The ^{31}P NMR calculations in the chemically non-equivalent phosphates (Tab. S3) confirmed assignment of resonances in the measured ^{31}P NMR spectra (Fig. S3) due to the inner (sPs) and the $\text{NH}_2 5'$ -Ps and $\text{NH}_2 3'$ -Ps phosphates.

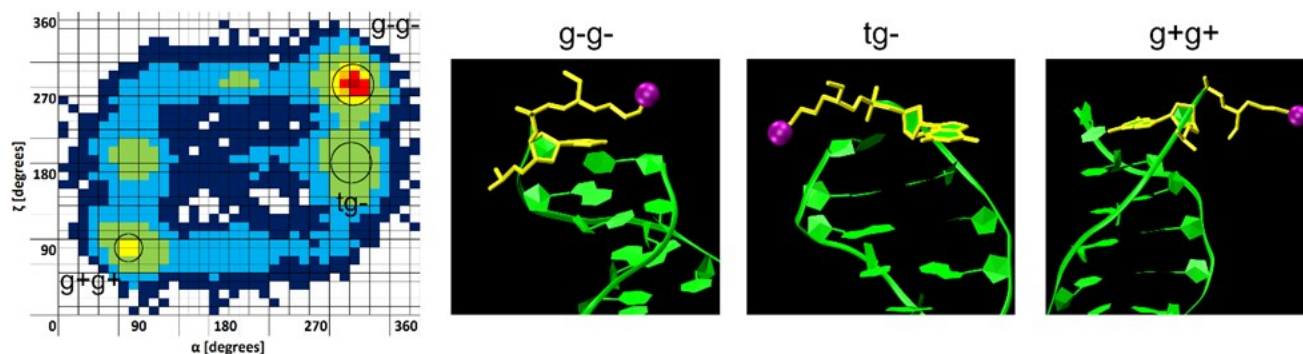


Figure S25. Three principal orientations of NH_2 -linker relative to the 3' phosphate of the **dsDNA-NH₂** calculated with MD. The g^-g^- , tg^- and g^+g^+ conformers were due to particular orientations of ζ and α torsion angles within the 3'-phosphate (Fig. S24). Gradual increase of occurrences of MD snapshots within the 10×10 grid points (left) was indicated by blue-green-yellow-red range of colors. NH_2 group in the three representative conformers is depicted as magenta ball.

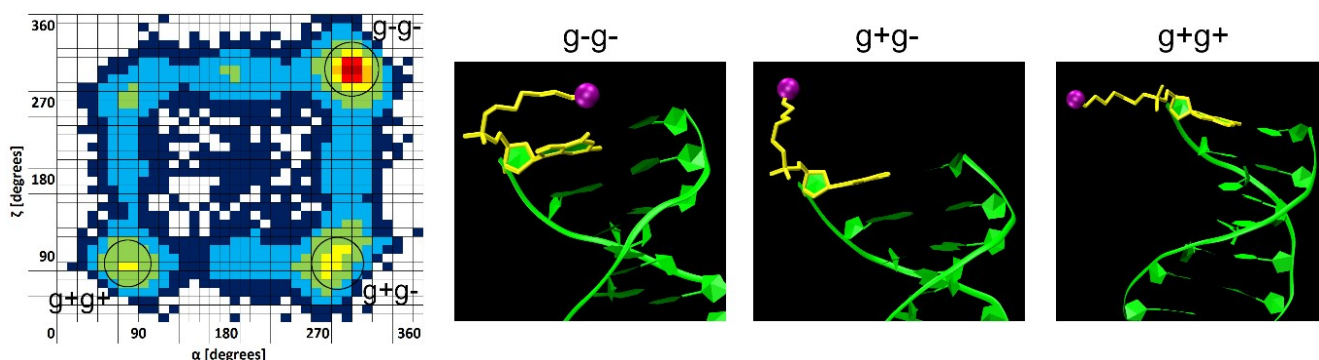


Figure S26. Three principal orientations of NH_2 -linker relative to the 5' phosphate of the **dsDNA-NH₂** calculated with MD. The g^-g^- , g^+g^- and g^+g^+ conformers were due to particular orientations of ζ and α torsion angles within the 5'-phosphate (Fig. S24). Gradual increase of occurrences of MD snapshots within the 10×10 grid points (left) was indicated by blue-green-yellow-red range of colors. NH_2 group in the three representative conformers is depicted as magenta ball.

The problem of computational complexity of MJs containing DNA molecules has been tackled in the past by Mohammad *et al.*³⁵ Authors computed MJ transmission functions without considering gold electrode clusters and anchoring groups explicitly. Instead they introduced the coupling strength parameter Γ of a fixed value. Following this approach, we used MD simulation of DNA without electrodes as a

basis for modelling of transmission functions of **ssDNA-NH₂** and **dsDNA-NH₂** systems. We have taken eleven snapshots at 0 ns, 10 ns, 20 ns, 30 ns, 40 ns, 50 ns, 60 ns, 70 ns, 80 ns (for double stranded DNA the snapshot was taken at 79,992 ns time of MD simulation due to a problem with SCF convergence of DFT-B3LYP calculation), 90 ns and 100 ns of the simulation time. The water molecules of all 11 geometries were removed and Na⁺ ions were manually shifted to the vicinity of the phosphate groups to neutralize their negative charge. Such system was geometrically optimized using PM7 method (Gaussian 16 program)²² where only Na⁺ ions were not constrained at their xyz coordinates. Resulted geometries were used for molecular orbital energies calculations using DFT-B3LYP method with the basis set 6-31G(d); the implicit solvent (water) was calculated using Polarizable Continuum Model as implemented in Gaussian 16. Transmission functions of single stranded and double stranded DNA were calculated using the equation³⁶

$$T(E) = \frac{\Gamma_L^{HOMO} \Gamma_R^{HOMO}}{(E - E_{HOMO})^2 + (\Gamma_L^{HOMO} + \Gamma_R^{HOMO})^2} + \frac{\Gamma_L^{LUMO} \Gamma_R^{LUMO}}{(E - E_{LUMO})^2 + (\Gamma_L^{LUMO} + \Gamma_R^{LUMO})^2} \quad (1)$$

where all Γ coupling strengths were fixed at one value $\Gamma = \Gamma_L^{HOMO} = \Gamma_R^{HOMO} = \Gamma_L^{LUMO} = \Gamma_R^{LUMO}$. In other words, we supposed that DNA frontier orbitals interact with the gold electrode orbitals in a symmetrical way. We tested several coupling strength values including 10 meV (low coupling strength), 20 meV, 50 meV and 100 meV (high coupling strength). The energies E_{HOMO} and E_{LUMO} are HOMO and LUMO energies of our MD snapshot system calculated by DFT-B3LYP method. We used E_F value of -4.7 eV for aqueous environment.³⁷ Further, we assumed that not only one frontier orbital can contribute to the charge transport pathway, but several others that are close in the energy. We used five highest lying occupied orbitals and five lowest lying unoccupied frontier orbitals to obtain transmission function of the molecular junction. These orbitals are shown in Figs. S27 and S28. The values of energies of frontier molecular orbitals are summarized in Tabs. 4 and 5.

Each transmission function of given MD snapshot geometry j was calculated as sum of individual contributions from HOMO and LUMO states, HOMO-1 and LUMO+1 states, HOMO-2 and LUMO+2 states, HOMO-3 and LUMO+3 states and HOMO-4 and LUMO+4 states according to the equation

$$T_j(E) = T(E) + \sum_{i=1}^4 \frac{4\Gamma^2}{(E - E_{HOMO-i})^2 + 4\Gamma^2} + \frac{4\Gamma^2}{(E - E_{LUMO+i})^2 + 4\Gamma^2} \quad (2)$$

Final transmission functions $\tau(E)$ depicted in Fig.S29 were calculated as an average from 11 transmission functions relevant for 11 MD snapshots according to the equation

$$\tau(E) = \frac{1}{n} \sum_{j=1}^n T_j(E) \quad (3).$$

Our analysis for 10 meV coupling strength value shows that **dsDNA-NH₂** has smaller LUMO-HOMO gap than corresponding **ssDNA-NH₂** model for all investigated geometries. The calculated ratio of conductance of double stranded versus single stranded DNA is 2.69, which is close to the distance-corrected value of 2.7 ± 0.5 for G_{dsDNA}/G_{ssDNA} ratio reported in the manuscript. The conductance ratio of double stranded versus single stranded DNA is strongly influenced by the energy difference between HOMO orbitals of DNA and the Fermi level, see Fig. S29.

Furthermore, we systematically changed Γ value (10 meV, 20 meV, 50 meV and 100 meV) for single stranded and double stranded DNA systems based on 100 ns MD snapshot, *i.e.* we calculated transmission functions for one snapshot geometry according to Eq. 2 for different Γ values. The G_{dsDNA}/G_{ssDNA} conductance ratio was almost unchanged (the ratio was 1.80 for 10 meV, 1.80 for 20 meV, 1.79 for 50 meV and 1.73 for 100 meV). We also tested the stability of G_{dsDNA}/G_{ssDNA} ratio for different number of frontier orbitals included in our calculations. For a two-state model (only HOMO and LUMO energies were included) we obtained the ratio 2.79, for the four-state model the ratio was 2.77, for the six-state model the ratio was 2.73, for the eight-state as well as the ten-state model (all five terms in Eq. 2) the conductance ratio was 2.69.

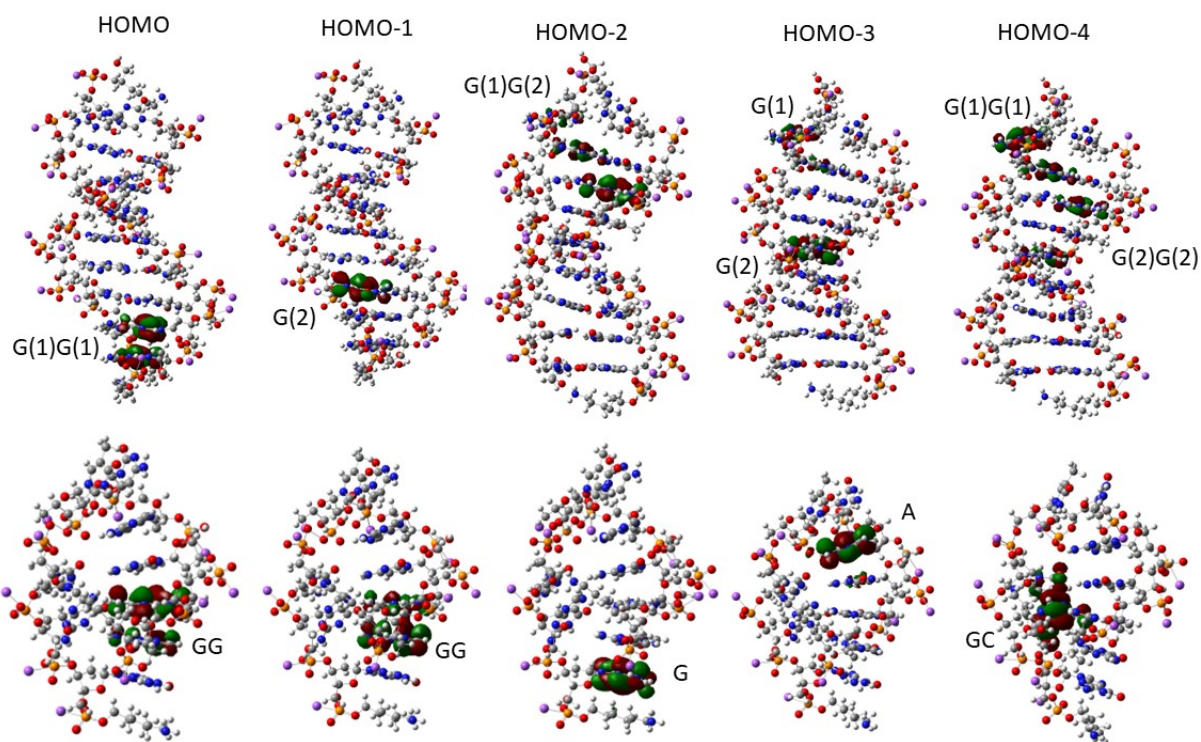


Figure S27. HOMO orbitals of **dsDNA-NH₂** (top panel) and **ssDNA-NH₂** (bottom panel) molecules. The shape distribution of MOs was calculated with isovalue 0.02. For dsDNA (top panel) number 1 in parentheses means the localization of DNA base on strand with linkers and anchoring groups, number 2 in parentheses the localization of DNA base on strand without linkers and anchoring groups (**ssDNA**).

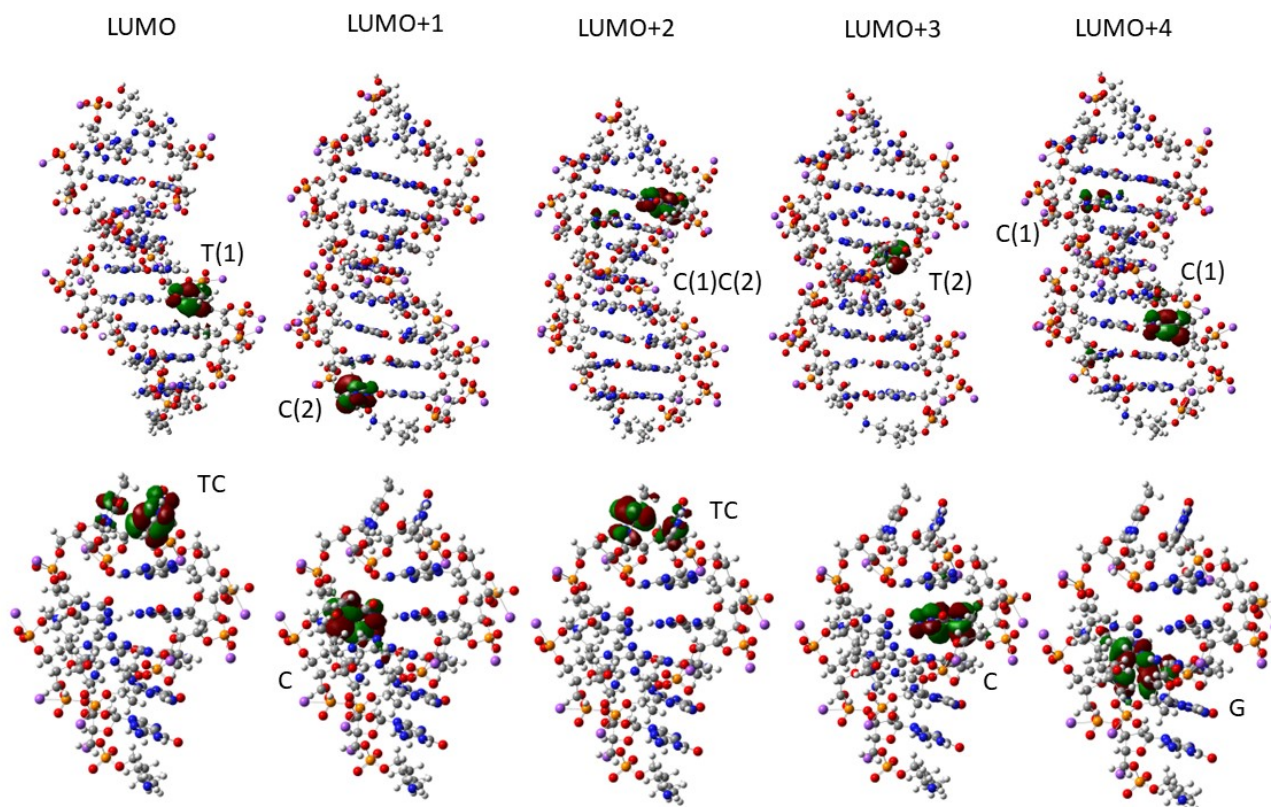


Figure S28. LUMO orbitals of **dsDNA-NH₂** (top panel) and **ssDNA-NH₂** (bottom panel) molecules. The shape distribution of MOs was calculated with isovalue 0.02. For dsDNA (top panel) number 1 in parentheses means the localization of DNA base on strand with linkers and anchoring groups, number 2 in parentheses the localization of DNA base on strand without linkers and anchoring groups (**ssDNA**).

Table S4. Summary of energies of 5 highest lying molecular orbitals and 5 lowest lying molecular orbitals and LUMO-HOMO difference for individual geometries based on MD snapshots of **ssDNA-NH₂** system. Orbital energies are given in eV.

Orbital	0 ns	10 ns	20 ns	30 ns	40 ns	50 ns	60 ns	70 ns	80 ns	90 ns	100 ns
HOMO	-5.245	-5.546	-5.240	-5.495	-5.474	-5.531	-5.543	-5.463	-5.520	-5.539	-5.235
HOMO-1	-5.283	-5.700	-5.437	-5.551	-5.625	-5.618	-5.705	-5.485	-5.683	-5.573	-5.547
HOMO-2	-5.683	-5.817	-5.659	-5.614	-5.627	-5.706	-5.751	-5.597	-5.761	-5.652	-5.752
HOMO-3	-5.799	-5.844	-5.722	-5.681	-5.858	-5.724	-5.798	-5.744	-5.769	-5.712	-5.775
HOMO-4	-5.848	-5.885	-5.914	-5.711	-6.045	-5.954	-5.964	-6.028	-5.781	-5.804	-5.780
LUMO	-1.309	-1.137	-1.102	-0.967	-1.222	-1.290	-1.221	-1.164	-1.187	-1.182	-1.047
LUMO+1	-1.097	-0.922	-1.017	-0.913	-0.971	-1.035	-1.101	-1.098	-1.118	-1.092	-1.001
LUMO+2	-0.843	-0.890	-0.783	-0.749	-0.791	-0.896	-0.965	-0.765	-0.821	-0.848	-0.799
LUMO+3	-0.709	-0.731	-0.617	-0.728	-0.726	-0.692	-0.849	-0.564	-0.806	-0.659	-0.701
LUMO+4	-0.692	-0.549	-0.556	-0.456	-0.589	-0.586	-0.462	-0.380	-0.601	-0.547	-0.615
LUMO-HOMO gap	3.936	4.409	4.139	4.529	4.252	4.241	4.322	4.299	4.333	4.357	4.189

Table S5. Summary of energies of 5 highest lying molecular orbitals and 5 lowest lying molecular orbitals and LUMO-HOMO difference for individual geometries based on MD snapshots of **dsDNA-NH₂** system. Orbital energies are given in eV.

Orbital	0 ns	10 ns	20 ns	30 ns	40 ns	50 ns	60 ns	70 ns	80 ns	90 ns	100 ns
HOMO	-4.995	-5.150	-5.168	-5.127	-5.213	-5.182	-5.227	-5.176	-5.052	-5.038	-5.156
HOMO-1	-5.115	-5.187	-5.195	-5.129	-5.294	-5.335	-5.228	-5.380	-5.087	-5.149	-5.325
HOMO-2	-5.148	-5.405	-5.306	-5.258	-5.346	-5.399	-5.392	-5.389	-5.215	-5.275	-5.342
HOMO-3	-5.350	-5.407	-5.401	-5.313	-5.351	-5.405	-5.401	-5.406	-5.277	-5.326	-5.406
HOMO-4	-5.552	-5.441	-5.405	-5.550	-5.416	-5.410	-5.423	-5.454	-5.339	-5.415	-5.418
LUMO	-1.234	-1.292	-1.149	-1.337	-1.227	-1.257	-1.159	-5.176	-1.312	-1.225	-1.493
LUMO+1	-1.177	-1.247	-1.147	-1.142	-1.211	-1.123	-1.080	-1.447	-1.304	-1.220	-1.379
LUMO+2	-1.023	-1.216	-1.110	-1.139	-1.132	-1.084	-1.036	-1.290	-1.220	-1.148	-1.141
LUMO+3	-1.007	-1.098	-1.046	-1.128	-1.096	-1.048	-1.016	-1.208	-1.026	-0.941	-1.106
LUMO+4	-0.969	-1.063	-1.012	-1.030	-1.028	-1.033	-0.952	-1.141	-0.999	-0.874	-0.967
LUMO-HOMO gap	3.761	3.858	4.019	3.790	3.986	3.925	4.069	3.729	3.740	3.813	3.663

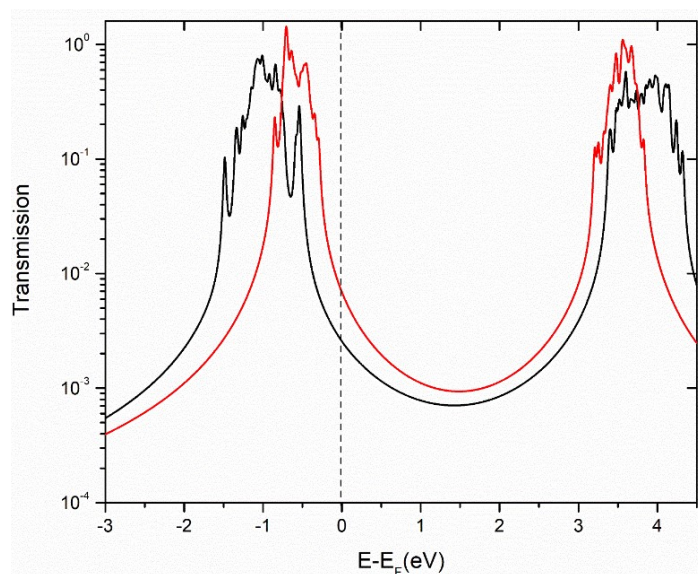


Figure S29. Transmission function $\tau(E)$ for **dsDNA-NH₂** (red) and **ssDNA-NH₂** (black) junction modelled as average of 11 transmission functions (based on 11 MD snapshots) using the energy of 5 highest lying molecular orbitals and energy of 5 lowest lying molecular orbitals (see Tab. 4 and 5) and using the value of coupling strength 10 meV. Vertical dashed line represents $E_F = -4.7$ eV.

7. STM BJ characteristics of DNA with one anchoring group on the oligonucleotide chain

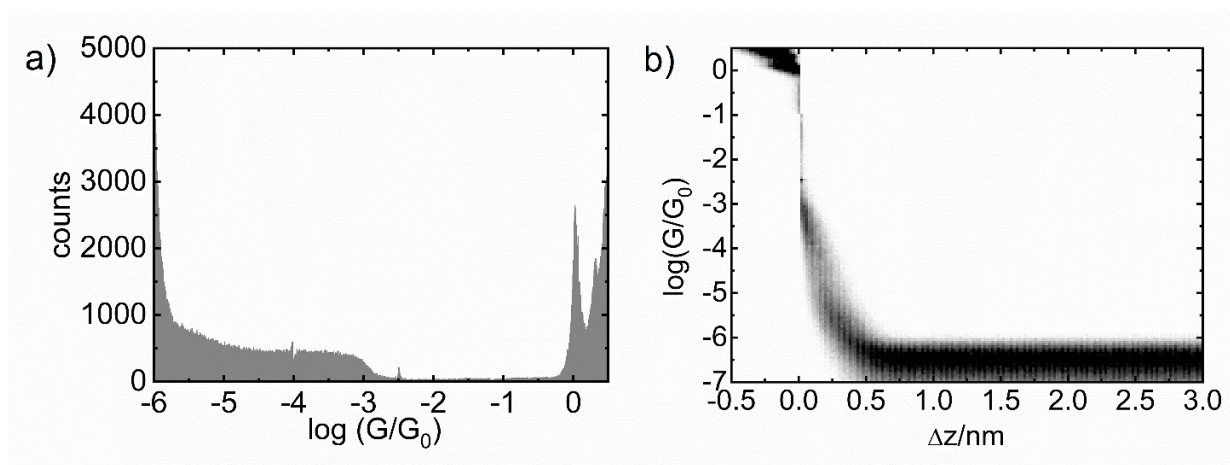


Figure S30. 1D logarithmic conductance (a) and 2D logarithmic conductance-distance (b) histogram for **H₂N-(CH₂)₆-5'-GGCTCACGG-3'** in D₂O. Tip retraction rate was 36 nm s⁻¹.

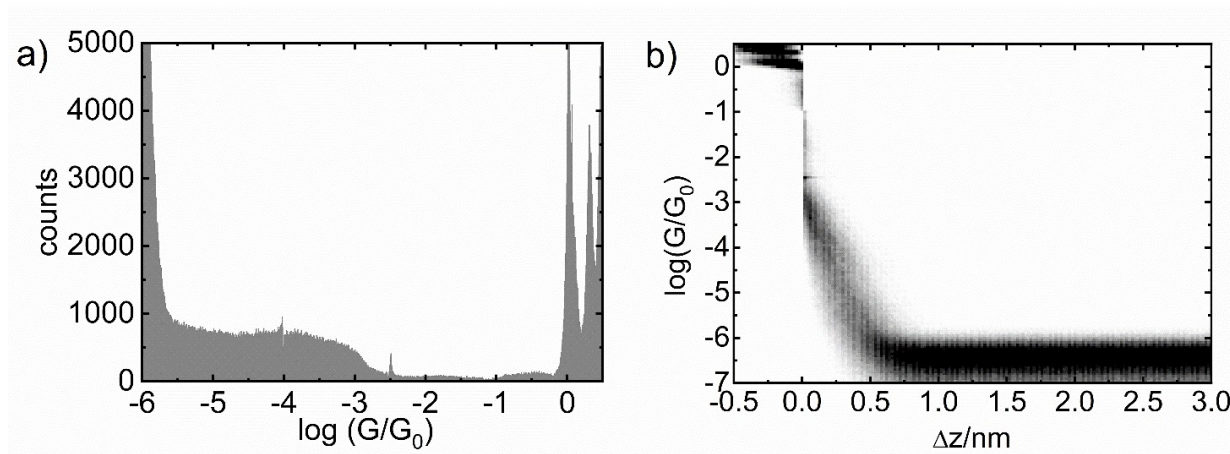


Figure S31. 1D logarithmic conductance (a) and 2D logarithmic conductance-distance (b) histogram for **H₂N-(CH₂)₆-5'-CCGAGTGCC-3'** in D₂O. Tip retraction rate was 36 nm s⁻¹.

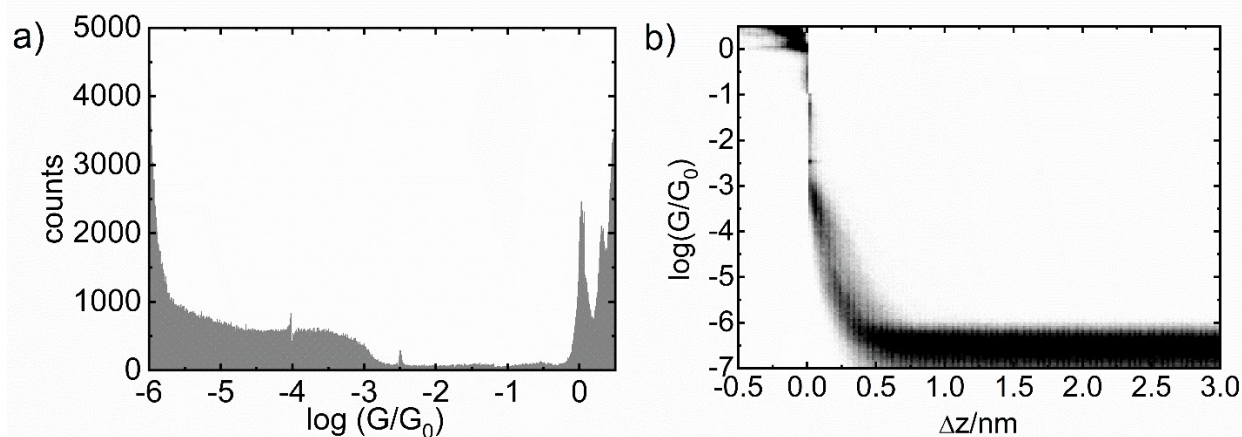


Figure S32. 1D logarithmic conductance (a) and 2D logarithmic conductance-distance (b) histogram for 1:1 mixture of $\text{H}_2\text{N}-(\text{CH}_2)_6\text{-5'-GGCTACGG-3'}$ and $\text{H}_2\text{N}-(\text{CH}_2)_6\text{-5'-CCGAGTGC-3'}$ in D_2O . Tip retraction rate was 36 nm s^{-1} .

8. References

- [1] C. D. Bain, H. A. Biebuyck and G. M. Whitesides, *Langmuir* 1989, **5**, 723.
- [2] J. Kypr, I. Kejnovská, K. Bednářová and M. Vorlíčková in *Comprehensive Chiroptical Spectroscopy: Applications in Stereochemical Analysis of Synthetic Compounds, Natural Products, and Biomolecules.*, Vol. 2, eds. N. Berova, P. L. Polavarapu, K. Nakanishi and R. W. Woody, John Wiley & Sons, Hoboken (NJ, USA), 2012, pp. 575–586.
- [3] J. Šebera, V. Kolivoška, M. Valášek, J. Gasior, R. Sokolová, G. Mészáros, W. Hong, M. Mayor and M. Hromadová, *J. Phys. Chem. C* 2017, **121**, 12885.
- [4] G. Mészáros, Ch. Li, I. V. Pobelov and T. Wandlowski, *Nanotechnology* 2007, **18**, 424004.
- [5] V. Kolivoška, M. Mohos, I. Pobelov, S. Rohrbach, K. Yoshida, W. Hong, Y. Fu, P. Moreno-Garcia, G. Mészáros and P. Broekmann, *Chem. Commun.* 2014, **50**, 11757.
- [6] I. V. Pobelov, M. Mohos, K. Yoshida, V. Kolivoska, A. Avdic, A. Lugstein, E. Bertagnolli, K. Leonhardt, G. Denuault and B. Gollas, *Nanotechnology* 2013, **24**, 115501.
- [7] G. Seifert, *J. Phys. Chem. A* 2007, **111**, 5609.
- [8] S. Datta, *Superlattices and microstructures* 2000, **28**, 253.
- [9] M. Ghorbani-Asl, *Electronic transport through two-dimensional transition-metal chalcogenides*, PhD thesis, Jacobs University, Bremen, Germany, 2014.
- [10] R. Rüger, A. Yakovlev, P. Philipsen, S. Borini, P. Melix, A.F. Oliveira, M. Franchini, T. van Vuren, T. Soini, M. de Reus, M. Ghorbani Asl, T. Q. Teodoro, D. McCormack, S. Patchkovskii, T. Heine *AMS DFTB 2021.1, SCM*, Theoretical Chemistry, Vrije Universiteit, Amsterdam, the Netherlands, <http://www.scm.com>.
- [11] a) D. Van Der Spoel, E. Lindahl, B. Hess, G. Groenhof, A. E. Mark and H. J. Berendsen, *J. Comput. Chem.* 2005, **26**, 1701; b) H. J. Berendsen, D. van der Spoel and R. van Drunen, *Comput. Phys. Commun.* 1995, **91**, 43; c) S. Pronk, S. Páll, R. Schulz, P. Larsson, P. Bjelkmar, R. Apostolov, M. R. Shirts, J. C. Smith, P. M. Kasson and D. van der Spoel, *Bioinformatics* 2013, **29**, 845.
- [12] M. M. Mariscal, O. A. Oviedo and E. P. M. Leiva, *Metal clusters and nanoalloys: from modeling to applications*, Springer Science & Business Media, 2012.
- [13] Z. Futera and J. Blumberger, *J. Chem. Theory Comput.* 2018, **15**, 613.
- [14] R. Dennington, T. Keith and J. Millam, *GaussView, version 5*, 2009.
- [15] Computer program *Maestro, version 9.3*, Schrödinger, LLC, New York, 2012.
- [16] S. Grimme, C. Bannwarth and P. Shushkov, *J. Chem. Theory Comput.* 2017, **13**, 1989.
- [17] a) S. Datta, *Electronic transport in mesoscopic systems*, Cambridge university press, 1997; b) R. Landauer, *J. Phys. Condens. Matter* 1989, **1**, 8099.
- [18] M. Wahiduzzaman, A. F. Oliveira, P. Philipsen, L. Zhechkov, E. van Lenthe, H. A. Witek and T. Heine, *J. Chem. Theory Comput.* 2013, **9**, 4006.
- [19] a) T. Heine, *Acc. Chem. Res.* 2015, **48**, 65; b) M. Ghorbani-Asl, A. Kuc, P. Miró and T. Heine, *Adv. Mater.* 2016, **28**, 853.
- [20] a) Z. Vokacova, M. Budesinsky, I. Rosenberg, B. Schneider, J. Sponer and V. Sychrovsky, *J. Phys. Chem. B* 2009, **113**, 1182; b) H. A. Gabb, S. R. Sanghani, C. H. Robert and C. Prevost, *J. Mol. Graph.* 1996, **14**, 6.
- [21] A. D. Becke, *J. Chem. Phys.* 1993, **98**, 5648.
- [22] M. J. Frisch, G. W. Trucks, H. B. Schlegel, G. E. Scuseria, M. A. Robb, J. R. Cheeseman, G. Scalmani, V. Barone, G. A. Petersson, H. Nakatsuji, X. Li, M. Caricato, A. V. Marenich, J. Bloino, B. G. Janesko, R. Gomperts, B. Mennucci, H. P. Hratchian, J. V. Ortiz, A. F. Izmaylov, J. L. Sonnenberg, D. Williams-Young, F. Ding, F. Lipparini, F. Egidi, J. Goings, B. Peng, A. Petrone, T. Henderson, D. Ranasinghe, V. G. Zakrzewski, J. Gao, N. Rega, G. Zheng, W. Liang, M. Hada, M. Ehara, K. Toyota, R. Fukuda, J. Hasegawa, M. Ishida, T. Nakajima, Y. Honda, O. Kitao, H. Nakai, T. Vreven, K. Throssell, J. A. Montgomery, Jr., J. E. Peralta, F. Ogliaro, M. J. Bearpark, J. J. Heyd, E. N. Brothers, K. N. Kudin, V. N. Staroverov, T. A. Keith, R. Kobayashi, J. Normand, K. Raghavachari, A. P. Rendell, J. C. Burant, S. S. Iyengar, J. Tomasi, M. Cossi, J. M. Millam, M. Klene, C. Adamo, R. Cammi, J. W. Ochterski, R. L. Martin, K. Morokuma, O. Farkas, J. B. Foresman and D. J. Fox, *Gaussian 16, Revision C.01*, Gaussian, Inc., Wallingford CT, 2016.
- [23] M. M. Frandl, W. J. Pietro, W. J. Hehre, J. S. Binkley, M. S. Gordon, D. J. DeFrees and J. A. Pople, *J. Chem. Phys.* 1982, **77**, 3654.
- [24] P. J. Hay and W. R. Wadt, *J. Chem. Phys.* 1985, **82**, 299.
- [25] W. M. Schosser, L. A. Zotti, J. C. Cuevas and F. Pauly, *J. Chem. Phys.* 2019, **150**, 174705.
- [26] D.A. Case, V. Babin, J.T. Berryman, R.M. Betz, Q. Cai, D.S. Cerutti, T.E. Cheatham, III, T.A. Darden, R.E. Duke, H. Gohlke, A.W. Goetz, S. Gusarov, N. Homeyer, P. Janowski, J. Kaus, I. Kolosváry, A. Kovalenko, T.S. Lee, S. LeGrand, T. Luchko, R. Luo, B. Madej, K.M. Merz, F. Paesani, D.R. Roe, A. Roitberg, C. Sagui, R. Salomon-Ferrer, G. Seabra, C.L. Simmerling, W. Smith, J. Swails, R.C. Walker, J. Wang, R.M. Wolf, X. Wu and P.A. Kollman, *AMBER 14*, University of

California, San Francisco, 2014.

- [27] M. Zgarbova, J. Sponer, M. Otyepka, T. E. Cheatham, R. Galindo-Murillo and P. Jurecka, *J. Chem. Theory Comput.* 2015, **11**, 5723.
- [28] a) T. Clark, J. Chandrasekhar, G. W. Spitznagel and P. V. Schleyer, *J. Comput. Chem.* 1983, **4**, 294; b) P. C. Hariharan and J. A. Pople, *Theor. Chim. Acta* 1973, **28**, 213.
- [29] M. J. Frisch, G. W. Trucks, H. B. Schlegel, G. E. Scuseria, M. A. Robb, J. R. Cheeseman, G. Scalmani, V. Barone, B. Mennucci, G. A. Petersson, H. Nakatsuji, M. Caricato, X. Li, H. P. Hratchian, A. F. Izmaylov, J. Bloino, G. Zheng, J. L. Sonnenberg, M. Hada, M. Ehara, K. Toyota, R. Fukuda, J. Hasegawa, M. Ishida, T. Nakajima, Y. Honda, O. Kitao, H. Nakai, T. Vreven, J. A. Montgomery, Jr., J. E. Peralta, F. Ogliaro, M. Bearpark, J. J. Heyd, E. Brothers, K. N. Kudin, V. N. Staroverov, R. Kobayashi, J. Normand, K. Raghavachari, A. Rendell, J. C. Burant, S. S. Iyengar, J. Tomasi, M. Cossi, N. Rega, J. M. Millam, M. Klene, J. E. Knox, J. B. Cross, V. Bakken, C. Adamo, J. Jaramillo, R. Gomperts, R. E. Stratmann, O. Yazyev, A. J. Austin, R. Cammi, C. Pomelli, J. W. Ochterski, R. L. Martin, K. Morokuma, V. G. Zakrzewski, G. A. Voth, P. Salvador, J. J. Dannenberg, S. Dapprich, A. D. Daniels, Ö. Farkas, J. B. Foresman, J. V. Ortiz, J. Cioslowski and D. J. Fox, *Gaussian 09 Rev. D.01*, Gaussian, Inc., Wallingford CT, 2009.
- [30] a) C. T. Lee, W. T. Yang and R. G. Parr, *Phys. Rev. B* 1988, **37**, 785; b) S. H. Vosko, L. Wilk and M. Nusair, *Can. J. Phys.* 1980, **58**, 1200; c) P. J. Stephens, F. J. Devlin, C. F. Chabalowski and M. J. Frisch, *J. Phys. Chem.* 1994, **98**, 11623.
- [31] R. Ditchfield, W. J. Hehre and J. A. Pople, *J. Chem. Phys.* 1971, **54**, 724.
- [32] A. V. Marenich, C. J. Cramer and D. G. Truhlar, *J. Phys. Chem. B* 2009, **113**, 6378.
- [33] W. Kutzelnigg, U. Fleischer and M. Schindler in *NMR – Basis Principles and Progress*, Vol. 213, Springer, Verlag, Berlin/Heidelberg, 1991.
- [34] J. Fukal, M. Buděšínský, O. Páv, P. Jurečka, M. Zgarbová, J. Šebera and V. Sychrovský, *J. Comput. Chem.* 2021, **43**, 132.
- [35] H. Mohammad, B. Demir, C. Akin, B. Luan, J. Hihath, E. E. Oren and M. P. Anantram, *Nanoscale Horiz.* 2021, **6**, 651.
- [36] M. Hromadová and V. Kolivoška in *Encyclopedia of Interfacial Chemistry: Surface Science and Electrochemistry*, Vol. 5, ed. K Wandelt, Elsevier, 2018, pp. 271–280.
- [37] Š. Nováková Lachmanová, V. Kolivoška, J. Šebera, J. Gasior, G. Mészáros, G. Dupeyre, P. P. Lainé and M. Hromadová, *Angew. Chem. Int. Ed.* 2021, **60**, 4732.